2

Dosimetry in Diagnostic Radiology and Computerized Tomography

CARL A. CARLSSON AND
GUDRUN ALM CARLSSON

DEPARTMENT OF RADIATION PHYSICS
FACULTY OF HEALTH SCIENCES
LINKÖPING UNIVERSITY
S-581 85 LINKÖPING, SWEDEN

I. Introduction

Illness implies a risk for the patient. An x-ray examination will contribute a small but finite increase in this risk. When a serious illness is discovered and an adequate treatment introduced, the patient's risk may be radically reduced (Edholm, 1982) (Fig. 1). Also, when the diagnosis excludes the presence of a serious disease, the benefit to the patient by far compensates the small radiation risk.

Even if the cost–benefit ratio is usually extremely favorable for the use of diagnostic x rays, the fact that diagnostic radiology is the largest man-made source of ionizing radiation to humans makes it important to find methods for utilizing the radiation as effectively as possible, i.e., maximizing the information-to-risk ratio. This is especially true when large screening programs with x rays are to be performed, such as mammography screening for breast cancer. Since risk increases with increasing absorbed dose, comprehensive dosimetry is necessary in such optimization studies.

In digital radiography with unsaturable detectors, the information increases as more x ray photons are detected (fixed spectrum). There is a tendency in digital radiography, including computerized tomography (CT), to increase the irradiation of the patients to obtain more detailed

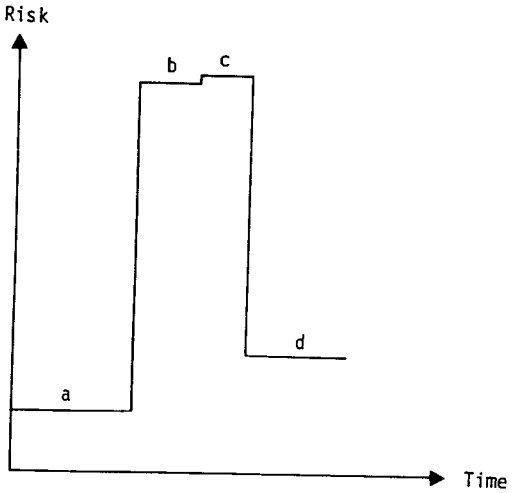

Fig. 1. Sketchy description of risk levels for patients in x-ray examinations: (a) normal risk level; (b) elevated risk due to illness; (c) increased risk due to x rays; (d) decreased risk due to successful diagnosis and treatment.

information. The development of powerful x-ray machines may create unsuspected opportunities to do so, but only at the cost of increased risks.

A. Radiation Risk and the Necessary Dosimetry

In order to quantify the deleterious effects of radiation, the International Commission on Radiological Protection (ICRP) has introduced the concepts of risk and detriment (ICRP, 1977a, 1984b, 1985). *Risk* is defined as the probability that an individual will incur a particular radiation-induced effect as a result of the distribution of the absorbed dose in the body. *Detriment* is defined as the mathematical expectation of the amount of harm to an exposed group of people, taking into account both the probability and the severity of the different possible harmful effects.

In diagnostic radiology, the absorbed doses in the patient are usually far below the thresholds for the occurrence of *nonstochastic* biological effects (ICRP, 1984a). The effects of main concern are those for which there is no evidence of a threshold absorbed dose, i.e., the *stochastic* effects of cancer induction, genetic injury, and developmental defects of the embryo and fetus (ICRP, 1986).

The concept of dose equivalent H was introduced to define the numerical relationship between values of absorbed dose and risk of stochastic effects at low absorbed doses. The dose equivalent is defined (ICRP, 1977a) as

$$H = DQN \tag{1}$$

where D is absorbed dose, Q is a quality factor which accounts for the different biological effectiveness of different types of radiation, and N is the product of all other modifying factors specified by the ICRP. At present, ICRP has assigned the value $N = 1$. The quality factor is defined as a function of the linear collision stopping power (L_∞) in water (ICRP, 1977a). Usually the absorbed dose is imparted by particles having a range of values of L_∞. For this case $\overline{Q}$ is calculated as an average of $Q(L_\infty)$ over all L_∞ with the absorbed dose as a weighting factor [International Commission on Radiation Units and Measurements (ICRU), 1980]. For the x rays used in diagnostic radiology, with electrons of various initial energies and L_∞ values, the ICRP recommends the value $\overline{Q} = 1$; that is, H and D have the same numerical values. Both are measured in units of joules per kilogram but have different special units, sievert (Sv) and gray (Gy), respectively.

Irradiations of the body with dose equivalents <1 Sv result in a total risk which is considered to be the sum of the risks associated with the individual irradiated organs. Assuming a linear relationship between risk and value of dose equivalent, the total risk can be expressed by a quantity, H_{eff}, obtained from a weighted sum of the organ mean dose equivalents $\overline{H}_T$ (Jacobi, 1975).

$$H_{\text{eff}} = \sum_T w_T \overline{H}_T \tag{2}$$

where the weighting factor w_T represents the ratio of the stochastic risk resulting from organ T to the total risk when the whole body is irradiated uniformly.

In recommending dose limitations for the protection of radiation workers, the ICRP (1977a) developed a set of w_T values (Table I) taking into account the risks for induction of fatal cancer and severe genetic injury to the two first generations of descendants. The quantity H_E derived from Eq. (2), using the w_T values in Table I, has been called the effective dose equivalent.

Although defined for a population of radiation workers, the effective dose equivalent H_E has been extensively used to estimate values of risk and detriment from diagnostic radiology. Values appropriate to patient populations are now being developed using sex- and age-dependent risk factors; see Fig. 2 (discussed in some detail in Section XI,B).

The evaluation of risks to the individual and detriment to the population from procedures of diagnostic radiology thus relies on the derivation

TABLE I

RISK WEIGHTING FACTORS FOR TISSUES[a]

Tissue	w_T
Gonads	0.25
Breast	0.15
Red bone marrow	0.12
Lung	0.12
Thyroid	0.03
Bone surfaces	0.03
Remainder	0.30

[a] Source: ICRP (1977a).

of mean absorbed doses (mean dose equivalents) in the body organs. A simpler procedure is to measure the energy imparted to the patient (see Section V), which, however, requires careful consideration of the relation between the mean absorbed dose in the total body and the risk-weighted quantity in Eq. (2) (Alm Carlsson and Carlsson, 1986). The energy imparted to the patient has the advantage of being independent of the modifying factors Q and N in Eq. (1) and the weighting factors w_T in Eq. (2). These are all humanly judged and may be changed repeatedly in the future (Greening, 1986). The energy imparted to the patient, or the absorbed dose averaged over the total body, may be the quantity of choice for dosimetric intercomparisons and optimization work.

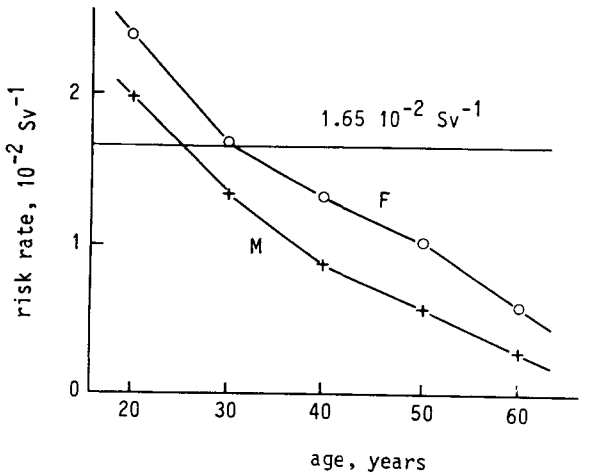

Fig. 2. Variation with age and sex of risk per unit dose equivalent (uniform whole-body irradiation), relative to the nominal value of 1.65×10^{-2} Sv^{-1} adopted for radiation protection purposes (ICRP, 1977a).

B. AIMS OF PATIENT DOSIMETRY

The absorbed doses in patients as well as in staff members have decreased during the last 30 years as a result of wise radiation-protection programs and improved technical equipment. On the other hand, the number of examinations has increased, which is why patient dosimetry remains a matter of concern. This chapter concentrates on patient dosimetry; however, a short presentation of staff dosimetry is also given (Section XIII).

There are two main objectives of patient dosimetry:

1. To know absorbed doses and risk levels in order to judge the impact of diagnostic radiology on public health and to prevent radiation phobia among individuals. For risk estimates, only crude dosimetry is needed.
2. To optimize the examination technique. Absorbed dose measurements in a standard phantom, radiographed at different hospitals, have revealed that the effective dose equivalent (risk) can vary more than a factor of 10 without a corresponding correlation with image quality. For optimization and comparisons of absorbed dose levels in different places or time periods, higher accuracy is desirable than is generally available today.

In work on optimization, the response, and thus the dosimetry of radiation detectors, is of basic importance. The dosimetry of radiation detectors is treated in Section IX and the problem of optimization in Section X.

II. Absolute Dosimetry of Diagnostic X Rays

Absolute dosimetry in the photon energy range 10–200 keV is based on determination of the quantities exposure, X, and air kerma, K_{air}. In this chapter the quantity air collision kerma, $K_{c,air}$ (Attix, 1979a,b), is used extensively. For x rays, collision kerma is equal to the absorbed dose under conditions of electronic equilibrium (Alm Carlsson, 1985). Exposure and collision kerma are related as

$$X = K_{c,air}\, e/W \tag{3}$$

and $K_c = K(1 - g)$, where e is the charge of an electron, W the mean energy needed to form an ion pair, and g the average fraction of the initial kinetic energy of the electrons lost to bremsstrahlung in slowing down. The quantities X, K_{air}, and $K_{c,air}$ can be determined at standardization

laboratories with good accuracy. It is also possible to calibrate practical dosemeters with high accuracy for well-determined x-ray spectra.

When the air collision kerma is measured, the collision kerma in tissue (medium) can be calculated from

$$K_{c,med} = \frac{(\overline{\mu_{en}/\rho})_{med}}{(\overline{\mu_{en}/\rho})_{det}} K_{c,det} \tag{4}$$

with air as the detector material. The mass energy absorption coefficients μ_{en}/ρ for medium and detector are weighted averages with the energy fluence Ψ (ICRU, 1980) as the weighting factor and $\Psi_{h\nu} = d\Psi(h\nu)/d(h\nu)$:

$$\frac{\overline{\mu_{en}}}{\rho} = \int_0^\infty \frac{\mu_{en}(h\nu)}{\rho} \Psi_{h\nu} \frac{1}{\Psi} d(h\nu) = \frac{K_c}{\Psi} \tag{5}$$

Within the range of energies (10–200 keV) used in diagnostic radiology, the mass attenuation and mass energy absorption coefficients μ/ρ and μ_{en}/ρ vary greatly with energy and atomic number (Hubbell, 1982). As a result, the energy distribution of the energy fluence changes with depth in a medium, with field area, with anode angle, and with the materials in the tube window and added filters.

With the photon energies used in x-ray examinations, electronic equilibrium conditions are usually fulfilled. This means that Eq. (4) can be used for determination of absorbed doses. Figure 3 shows the ratio $(\mu_{en}/\rho)_{det}/(\mu_{en}/\rho)_{med}$ as a function of photon energy for bone and the interesting dosimetric materials air, $Li_2B_4O_7$, LiF, and photographic emulsion (as representative for "detectors") with soft tissue as the normalizing medium (data from Hubbell, 1982).

If absorbed doses in a tissue or medium are determined with dosimeters, as tissue-equivalent as possible (see Section III), the errors in transferring the absorbed dose (collision kerma) in a detector to that in the medium are minimized. For measurement of absorbed doses in soft tissue, air and $Li_2B_4O_7$ are very suitable materials and even LiF is reasonably good (Fig. 3).

Equation (4) implies that attenuation in the detector can be neglected. Practical detectors (of finite size) are often calibrated under scatter-free conditions to measure, for example, $K_{c,air}$. When used within a phantom, differences in attenuation and scattering of the x rays in phantom and detector complicate the dosimetry. The use of a low-density detector, such as an air-filled ionization chamber of relatively large volume, to measure depth doses in phantoms has caused overestimates. This was suspected by Carlsson (1963), based on the analysis by Lidén (1961), and was experimentally shown by Harrison (1981). The use of dosimeters of

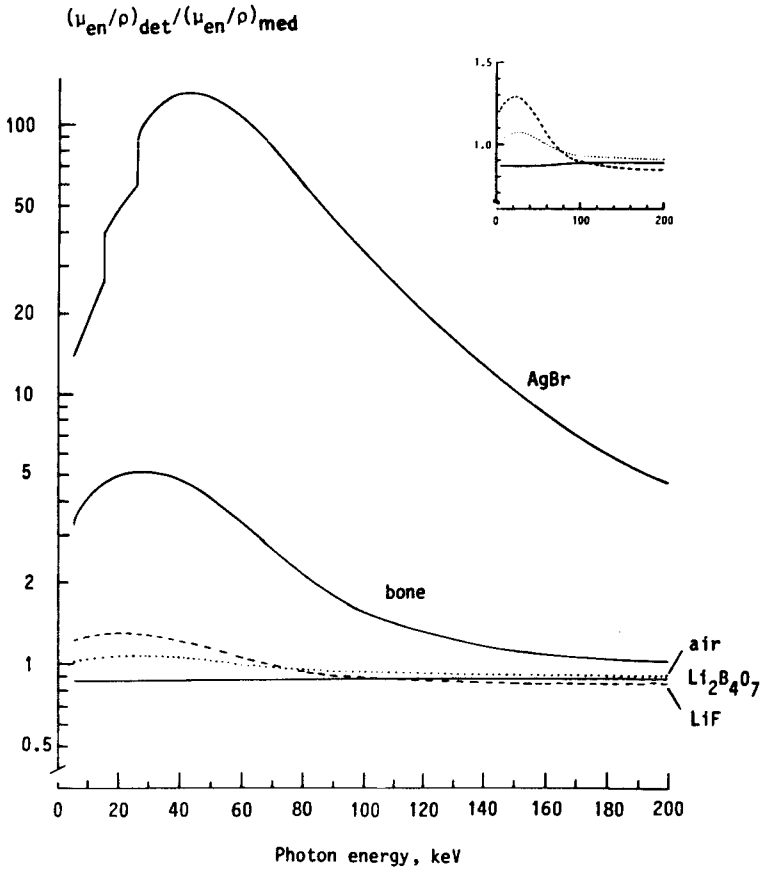

Fig. 3. Mass energy absorption coefficients of some dosimeter materials and bone, relative to that of soft tissue. The inset shows LiF, air, and $Li_2B_4O_7$ with an expanded linear scale.

higher density than the surrounding materials, e.g., LiF in tissue-equivalent phantoms, introduces similar problems, especially with the low-energy photons used in mammography. Another problem, not satisfactorily solved, occurs if the variation in efficiency of thermoluminescent (TL) LiF with the linear energy transfer (LET) distribution of the electrons is so large that it requires correction (Rudén, 1976). This effect and light attenuation in the TL dosimeter (Rudén and Bengtsson, 1977) are probably of most importance at low x-ray and electron energies, where the gradient of absorbed dose within the dosimeter may be appreciable. As is evident from the above discussion, application of Eq. (4) (valid under the

idealized condition of identical energy fluence of photons throughout the detector and at the point of measurement in the medium) may require perturbation corrections for highly accurate dosimetry [Alm Carlsson, 1985, 1990; International Atomic Energy Agency (IAEA), 1987], as in radiotherapy applications.

III. Effective Energy and Effective Atomic Number

A. Effective Energy

It is tedious to evaluate equations like Eq. (5) and thus tempting to use some sort of effective energy. An effective energy for an energy distribution can be defined as the single energy that gives the same result as the actual energy distribution (Alm Carlsson and Carlsson, 1984). Equation (5) can be written as

$$(\overline{\mu_{en}/\rho})\,\Psi = K_c \tag{6}$$

When Ψ and K_c are determined, the effective photon energy $h\nu_{eff}$ is defined by

$$\overline{\mu_{en}/\rho} = \mu_{en}(h\nu_{eff,Kc})/\rho \tag{7}$$

This effective energy, determined from Eqs. (6) and (7), is valid only for determination of K_c. For attenuation, an effective energy of an x-ray spectrum is often based on the half-value thickness (HVT) or half-value layer (HVL). The HVT is defined as the thickness of a specified material that reduces a specified physical quantity to half its initial value. It is most often used with one of the closely related quantities exposure and air collision kerma. The HVTs for these two quantities are identical and are usually written without a subscript:

$$\mathrm{HVT}_{K_{c,air}} \equiv \mathrm{HVT}_X \equiv \mathrm{HVT}$$

In general, HVT is obtained from

$$\frac{1}{2}K_{c,air} = \int_0^\infty \left(\frac{\mu_{en}}{\rho}\right)_{air} \Psi_{h\nu} e^{-\mu(h\nu)\mathrm{HVT}}\, d(h\nu)$$

$$= K_{c,air}\, e^{-\mu(h\nu_{eff,HVT})\mathrm{HVT}} \tag{8}$$

The effective energy based on HVT is then given by

$$\mu(h\nu_{eff,HVT}) = \ln 2/\mathrm{HVT} \tag{9}$$

and can be determined from measured values of HVT and tabulated linear attenuation coefficients.

The HVT, as well as the effective energy derived from it, is very sensitive to the physical quantity for which it is defined or measured. By using Φ or Ψ instead of $K_{c,air}$ in Eqs. (8) and (9), one may determine $h\nu_{eff,HVT}$ for the quantities fluence Φ and energy fluence Ψ. One usually gets

$$h\nu_{eff,\mathrm{HVT}_{K_{c,air}}} < h\nu_{eff,\mathrm{HVT}_\Phi} < h\nu_{eff,\mathrm{HVT}_\Psi} \tag{10}$$

The corresponding HVTs, with $K_{c,air}$, Φ, and Ψ as reference quantities, come in the same order. If the attenuation is extended to a value other than 1/2, for example, 1/10 (tenth-value thickness), the effective energies also change.

For therapeutic applications, central-axis depth doses are tabulated with HVT for $K_{c,air}$ as the only parameter to describe the energy spectrum of incident x rays (British Institute of Radiology, 1983). With the lower photon energies of diagnostic x rays, μ and μ_{en}/ρ both vary appreciably over the photon energies in the spectrum. For two different spectra with the same HVT and $h\nu_{eff,HVT}$ [Eq. (9)], the effective energies $h\nu_{eff,K_{c,air}}$ [Eqs. (6) and (7)] deviate (Fig. 4). Considerable errors can be introduced by using $h\nu_{eff,HVT}$ instead of $h\nu_{eff,K_{c,air}}$ for determining $K_{c,air}$ or Ψ (Section V,A,2) from Eq. (6) (Alm Carlsson and Carlsson, 1984). In diagnostic radiology the concept of HVT must be used with care.

Equation (8) gives a stringent definition of HVT. For measurement of HVT it is important to collimate the beam well (half angle $\leq 2°$) to get the same result as calculated in Eq. (8). When calculating HVT, it is correspondingly important to use the total attenuation coefficient including the contribution from coherent scattering. An earlier practice of regarding coherently scattered photons as primary photons gives calculated HVT values that are higher than measured ones.

B. Effective Atomic Number

Analogously to effective energy, an effective atomic number of an object composed of different elements can be defined as the number Z_{eff} (not necessarily an integer) that gives the same result for a defined physical quantity as the summed effects of the different elements. Particular problems involved in deriving Z_{eff} are discussed below.

The concept of effective atomic number, exploited early by Mayneord (1937), was further developed by Spiers (1946) to account for the energy absorption of various body tissues compared to that of air and measured by means of the exposure. The idea was that interesting dosimetric quantities, e.g., the mass attenuation coefficient μ/ρ or the mass energy ab-

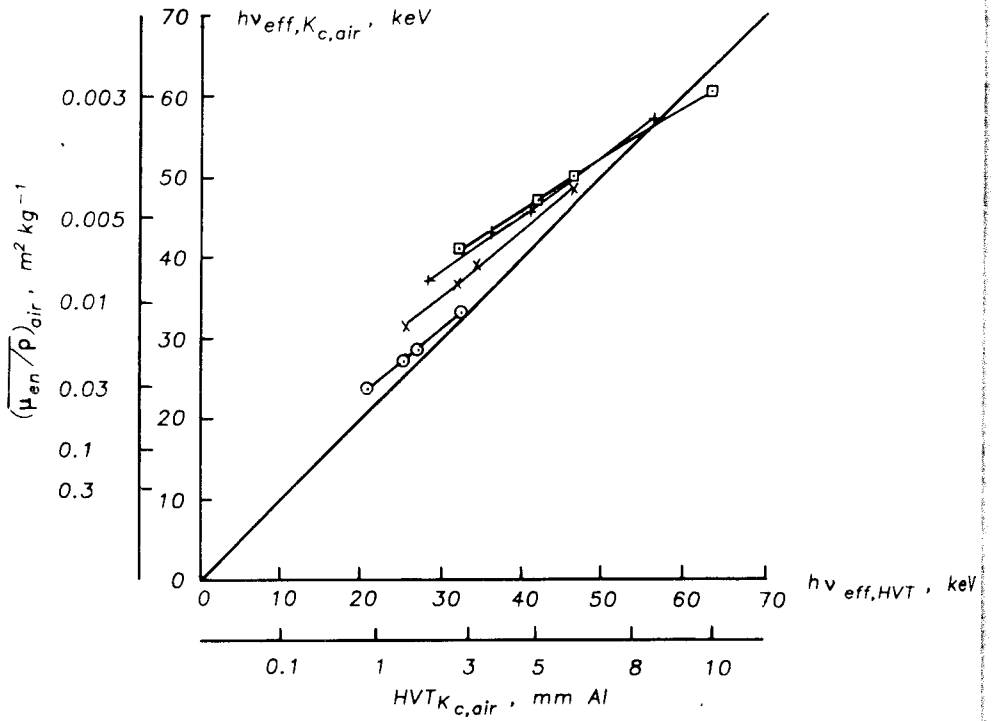

Fig. 4. Effective energy $h\nu_{\text{eff},K_{c,\text{air}}}$ as a function of $h\nu_{\text{eff,HVT}}$. Monoenergetic photons (solid line) and 40-kV (○), 70-kV (×), 100-kV (+), and 130-kV (□) energy spectra. Values of $(\overline{\mu_{en}/\rho})_{\text{air}}$ and $\text{HVT}_{K_{c,\text{air}}}$ are calculated from Eq. (6)–(9). [From Alm Carlsson and Carlsson (1984).]

sorption coefficient μ_{en}/ρ, can be derived for any tissue or compound, provided that certain constants are known, including the effective atomic number Z_{eff}.

The determination of an effective atomic number is, however, not unambiguous since it depends on the type of cross section used in its derivation (Henriksen and Baarli, 1957; Bradley *et al.*, 1986; Yang *et al.*, 1987). For instance, $(\mu/\rho)_c$ for a compound can be calculated in three ways (according to Bragg's additivity rule, neglecting effects of chemical binding):

$$(\mu/\rho)_c = \sum_i w_i(\mu/\rho)_i \tag{11a}$$

$$(\mu/\rho)_c = n_a\,{}_a\sigma_c = \sum_i n_{a,i}\,{}_a\sigma_i \tag{11b}$$

$$(\mu/\rho)_c = n_e\,{}_e\sigma_c = \sum_i n_{e,i}\,{}_e\sigma_i \tag{11c}$$

Here w_i is the fraction by weight of element i in the compound; n_a and n_e are the total numbers of atoms and electrons, respectively, per unit mass in the compound; $n_{a,i}$ and $n_{e,i}$ are the corresponding numbers of atoms and electrons of element i; and ${}_a\sigma_i$ and ${}_e\sigma_i$ are the total interaction cross sections per atom and per electron, respectively, for element i. From plots of μ/ρ, ${}_a\sigma$, and ${}_e\sigma$ as functions of Z, Z_{eff} is interpolated as the atomic number corresponding to $(\mu/\rho)_c$, ${}_a\sigma_c$, or ${}_e\sigma_c$ as demonstrated in Fig. 5.

As Fig. 5 shows, μ/ρ is not a monotonically varying function of Z and therefore is useless as a basis for determining an effective atomic number. The cross sections per atom or electron vary in a regular manner but yield two different values for Z_{eff}. In addition, when Compton scattering predominates such that ${}_e\sigma$ is independent of the atomic number, Z_{eff} as determined from Eq. (11c) is not unique. This will also be true when the plots of ${}_a\sigma$ and ${}_e\sigma$ versus Z contain absorption edges in the Z interval of interest (low photon energies, extended range of atomic numbers in the compound).

Spiers (1946) based his derivation of Z_{eff} on n_e and ${}_e\sigma$ [Eq. (11c)] but defined Z_{eff} for the partial process of photoelectric absorption only, utiliz-

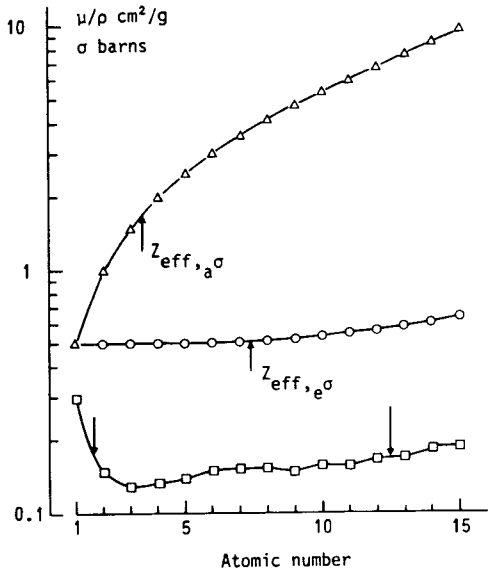

Fig. 5. Total interaction cross sections per unit mass μ/ρ (□), per atom ${}_a\sigma$ (△), and per electron ${}_e\sigma$ (○), as functions of atomic number for 100-keV photons. Arrows indicate effective atomic numbers Z_{eff} for H_2O with respect to the different sets of cross sections [Eqs. (11a)–(11c)]. Relating Z_{eff} to values of μ/ρ gives two different solutions, as shown by the lower curve. [Cross-section data from Storm and Israel (1970).]

ing a Z dependence of the form

$$ {}_e\sigma_{ph} = k(h\nu)Z^m \tag{12} $$

yielding

$$ (\mu/\rho)_c = n_e[{}_e\sigma_{sc} + k(h\nu)Z_{eff}^m] \tag{13} $$

where

$$ Z_{eff}^m = \sum_i (n_{e,i}/n_e)Z_i^m \tag{14} $$

and ${}_e\sigma_{sc}$ is the scattering cross section per electron, assumed to be independent of the atomic number.

The Z dependence in Eq. (12) has been utilized to determine effective atomic numbers for other partial processes as well. A problem is that the value of the exponent m varies among various authors, and m is also a function of photon energy (Weber and van den Berge, 1969; White, 1977a). Yang *et al.* (1987) arrived at slightly different values of Z_{eff} from Eq. (11c) when considering attenuation and energy absorption coefficients. The dependence of Z_{eff} on photon energy was found to be weak. On the contrary, Rao Thirumala *et al.* (1985) noticed a strong energy dependence in the interval 10–200 keV for Z_{eff} of various body tissues, basing their derivation on atomic cross sections [Eq. (11b)].

The concept of effective atomic number has found its principal application in the formulation of tissue-substitute materials for dosimetric phantoms. Difficulties in characterizing a compound with the single value of its effective atomic number were discussed in detail by White (1977b), who advocated instead a method based on basic interaction data. A compilation of tissue substitutes and their photon and electron interaction properties over the extended energy range 10 keV to 10 MeV was published by White (1978).

A reassessment of the composition of 30 selected adult human tissues has been made by White and Woodard (1988). They also give values of densities, electron stopping and scattering powers, and attenuation and energy absorption coefficients. This work has been further developed by the ICRU (ICRU, 1989).

Extensive tabulations of basic photon interaction cross sections as functions of energy are now available for all elements, $Z = 1$–100, as well as for a number of common compounds (Storm and Israel, 1970; Hubbell, 1982; Berger and Hubbell, 1987; Saloman *et al.*, 1988), facilitating a proper weighting over atomic composition and energy spectra for accurate dosimetry. Concepts such as effective energy and effective atomic number must be used with care or avoided. With access to extensive tables and a computer, it is better and safer to use all spectral and atomic information in solving dosimetry problems.

C. Effective Filter Thickness, Inherent Filtration

An inverse problem to the determination of an effective atomic number is to express the thickness of the x-ray tube window as an equivalent thickness of a given element (usually aluminum). Such equivalence requires, in general, that a change from the actual window to an equivalent Al window would result in the same HVT (International Electrotechnical Commission, 1976). The equivalent filtration of a given window depends on the energy spectrum and, with this definition, is smaller the steeper the anode angle.

Comparison of tabulated energy spectra (Birch *et al.*, 1979; Mika and Reiss, 1969; Reiss and Steinle, 1973) reveals problems in defining inherent filtration (Matscheko and Alm Carlsson, 1989b). In using tabulated spectra, it seems safer to depend on measured tube potential and HVT than on potential and total (inherent plus added) filtration (see Section V,3). The inherent filtration given by tube manufacturers is strictly valid for one spectrum (tube potential) only. Problems related to the concept of total filtration can be inferred from the careful measurements of HVT by Nagel (1988). With access to a Compton spectrometer (Yaffe *et al.*, 1976; Matscheko and Ribberfors, 1987, 1989; Matscheko, 1988; Matscheko and Alm Carlsson, 1989a,b; Matscheko *et al.*, 1989) it is comparatively easy to measure primary x-ray spectra. From the spectra, values of HVT can be calculated and compared to requirements of total filtration when this is needed (cf. Nagel, 1988).

IV. Interface and Cavity Dosimetry Problems

A. The General Interface Problem

The data in conventional tables of absorbed dose versus depth are determined by measurements in a homogeneous phantom of a soft-tissue substitute, e.g., water. In the patient, the various tissues in the body form interfaces between media of different energy absorption properties. Use of contrast agents (iodine, barium) introduces interfaces between soft tissues and media of high atomic number. Media of still higher atomic number, such as mercury (amalgam) and gold, may be present in the mouth.

At an interface between two media of different atomic numbers, a transition region exists where the electron fluence is due to secondary electrons released in both media and changes from the equilibrium fluence in one medium to the next (Fig. 6).

Since the maximum ranges of the secondary electrons released by 20–200-keV photons are $\leq 100\ \mu m$ in soft tissue, the transition region is small and only a few cell layers are affected. On the other hand, due to the strong increase of the photoelectric effect with increasing atomic number for low-energy photons, soft-tissue layers in contact with media of high atomic number receive a much higher absorbed dose than the equilibrium absorbed dose in soft tissue (Fig. 7). This is particularly a problem when artificial materials, such as titanium and stainless steel, are used for prostheses (Brånemark *et al.*, 1977).

Figure 7 shows experimentally determined absorbed dose distributions in the transition zone of a low-atomic-number medium [Mylar, $(C_{10}H_8O_4)_n$] in close contact with metal sheets of Al, Cu, Sn, and Pb irradiated with 100- and 200-kV x rays. The measurements were performed with 0.1-mm-thick thermoluminescent LiF–Teflon detectors. These totally absorb the secondary electrons (mainly photoelectrons) liberated in the metal sheets but are thin with respect to the mean free paths of the photons (including characteristic x rays from the metals). The absorbed dose distribution in Mylar was resolved by successively increasing the number of thin (0.486 mg cm^{-2}) Mylar films between the metal and the LiF–Teflon detector. The mean absorbed dose in Mylar foil number i was derived by subtracting the detector signal with $i - 1$ interposed films from that with i interposed films. The results are in good agreement with theoretical calculations developed by Spiers (1949, 1951), refined by Howarth (1965), and extended to high-Z media interfaces by Aspin and Johns (1963) and Charlton (1970), provided due account is taken of the electron multiple scattering (Roesch, 1954; Dutreix and Bernard, 1965; Cross, 1973) at the interface, which is neglected in the cited theories. Omission of electron multiple scattering leads to an overestimate of the calculated absorbed dose close to the planar interface. This increases with increasing atomic number, amounting to a factor of 2 for lead, but is nearly negligible for bone (Alm Carlsson, 1973). Monte Carlo calculations of absorbed dose distributions at plane metal–polyethylene (silicon) interfaces (Garth *et al.*, 1975; Chadsey, 1978) confirm the results derived from the Spiers theory combined with a multiple-scattering correction.

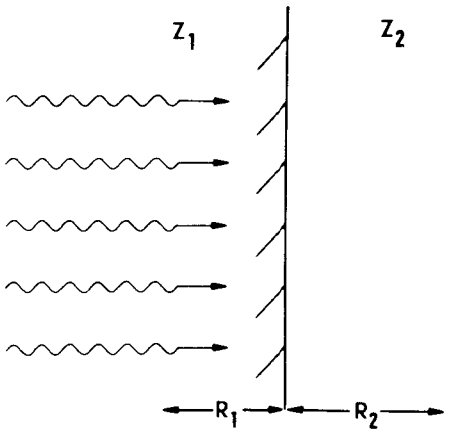

Fig. 6. Ranges of the most energetic secondary electrons, R_1 and R_2, define the transition region at an interface irradiated with roentgen rays. [From Alm Carlsson (1973).]

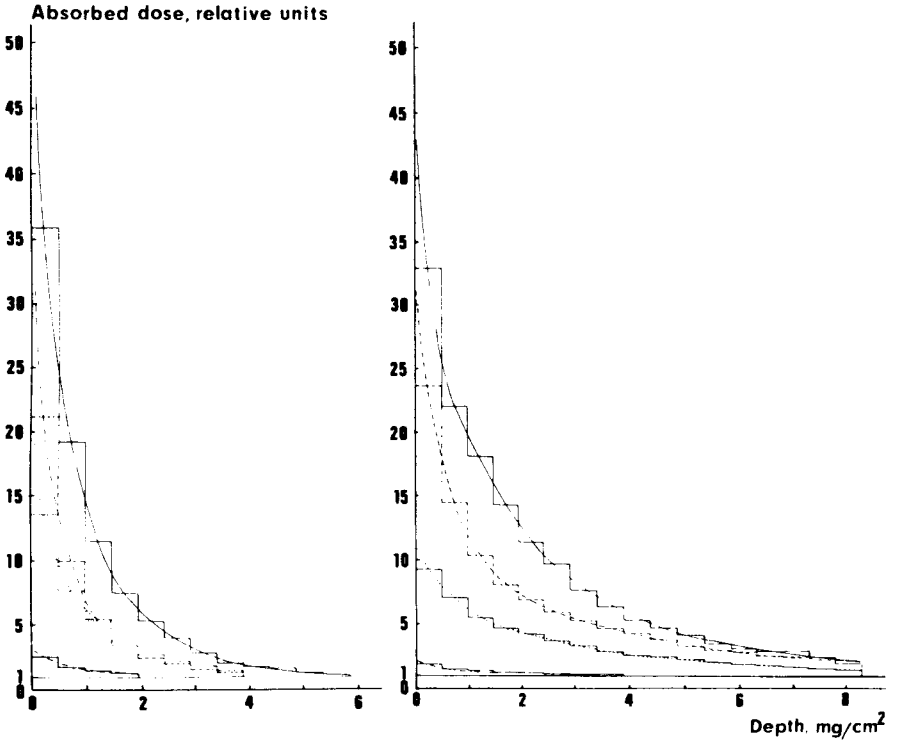

Fig. 7. Depth doses in Mylar from photoelectrons generated in an adjacent metal foil of Pb (———), Sn (----), Cu (····), and Al (-·-·-), irradiated with an x-ray beam of 100 kV (left) and 200 kV (right). The depth doses are normalized to the electronic equilibrium absorbed dose in LiF. The continuous curves are fitted to the histograms obtained experimentally. [From Alm Carlsson (1973).]

The subtraction technique used in the experiments in Fig. 7 requires high precision in the measurements. The relative standard deviation of the LiF–Teflon detector signal was 0.3%, using procedures for detector treatment described by Carlsson *et al.* (1968) and Mårtensson (1969). Measurements with a very thin dosimeter (thickness unspecified) have been made using thermally stimulated exoelectron emission (TSEE), discovered by Kramer. Kramer (1966) used TSEE dosimeters of BeO in direct contact with the same metals as in Fig. 7. There is good agreement between Kramer's results and the mean absorbed dose in the first Mylar films in Fig. 7. Ennow (1973) used LiF/C TSEE dosimeters, simulating the irradiation conditions of Alm Carlsson (1973). The resulting absorbed dose distributions were in good agreement.

High-quality measurements using an extrapolation chamber were performed with 30–210-kV x rays by Wingate *et al.* (1962). The measurements were limited to the simulation of planar interfaces between bone (or Pyrex glass) and soft tissue. It has long been recognized that red bone marrow, which is the sensitive organ for induction of leukemia and is contained within skeletal cavities, receives higher absorbed doses at these energies than soft tissues not in contact with bone (see the Al–Mylar interface in Fig. 7).

As long as the radius of curvature of an interface is large compared with the ranges of the secondary electrons, the planar interface offers a good model for determination of the absorbed dose distribution in the transition region. For many of the bone–marrow interfaces defined by bone cavities in the human skeleton, this approximation will not be valid.

B. Bone Marrow Dosimetry

Three types of soft tissues within the cavities of trabecular bone are considered especially vulnerable to the induction of malignant disease. For two of them, hematopoietic marrow and reticuloendothelial tissues, the quantity related to the radiation risk is the mean absorbed dose in the whole cavity. For the osteogenic tissues, it is the mean absorbed dose in a layer 10 μm thick lining the cavities.

Spiers (1949, 1951) was the first to develop a theory for calculating the absorbed dose in soft tissues in close contact with bone. He based his method on simplified assumptions about electron transport. The secondary electrons, released by the photons, were assumed to be emitted isotropically and to travel in straight lines from the point of emission, losing their energy continuously at a constant rate of stopping power. With these assumptions, Spiers was able to calculate the absorbed dose $D_m(P, T_0)$ in bone marrow at the point P from electrons of initial kinetic energy T_0. When the thickness of the adjacent bone structure is comparable to the maximum range of the electrons (which is the case for most of the trabecular bones when irradiated with photons of energies $\leq$200 keV), one has

$$D_m(P, T_0) = n_b T_0 \frac{R_b \rho_b}{R_m \rho_m} G(P, T_0) + n_m T_0 [1 - G(P, T_0)] \qquad (15)$$

Indices m and b stand for bone marrow and bone, respectively; n is the number of electrons with kinetic energy T_0 liberated per unit mass; R is the range along their assumed straight-line paths (taken to be 0.7 of the path length R_{csda} calculated in the continuous slowing-down approximation); and ρ is the density.

The two terms on the right-hand side in Eq. (15) give the contribution to $D_m(P, T_0)$ from electrons liberated by photons in bone and in bone marrow, respectively. $G(P, T_0)$ is a factor which depends on the geometry of the interface. For a point close to a plane interface, $G(P, T_0) = 0.5$. Furthermore, the quotient $R_b\rho_b/R_m\rho_m$ is assumed to be independent of T_0 and equal to the inverse ratio of the mass stopping powers of the electrons in bone and bone marrow. Thus, the absorbed dose in marrow at a plane interface equals the sum of half of the absorbed dose in a small (Bragg–Gray) marrow cavity within bone (electrons liberated in bone) and half of the absorbed dose in bone marrow in electronic equilibrium (electrons liberated in bone marrow).

Since electrons liberated by photons exhibit a spectrum of initial kinetic energies, Eq. (15) must be averaged over this energy spectrum to yield the absorbed dose in photon irradiations. The result is that nT_0 is replaced in Eq. (15) by K_c (collision kerma) and $G(P, T_0)$ by $\bar{G}(P)$.

The gradient of the absorbed dose at the interface, described by the geometric factor $\bar{G}(P)$, depends on the rate at which energy is imparted along the assumed straight-line electron paths. Spiers' original assumption, that this rate is constant, has been refined in calculations by Charlton and Cormack (1962), Howarth (1965), Charlton (1970), and Unnikrishnan (1977).

Since bone and bone marrow are not too different in atomic composition, effects of electron multiple scattering at the interface are small and the theory is in good agreement with experiments for plane interfaces (the geometry most easily tested) (Wingate *et al.*, 1962; Alm Carlsson, 1973).

In calculating the mean absorbed dose $\bar{D}_m$ in bone marrow within a trabecular cavity, Eq. (15) has to be averaged over both the position of point P in the cavity and the energy distribution of the released electrons

$$\bar{D}_m = K_{c,b} \frac{R_b \rho_b}{R_m \rho_m} \bar{\bar{G}} + K_{c,m}(1 - \bar{\bar{G}}) \qquad (16)$$

Here $\overline{\overline{G}}$ depends on the shape and dimension (relative to the electron ranges) of the cavity. To be exact, the values of $\overline{\overline{G}}$ may be somewhat different in the two terms of Eq. (16) when the energy spectra of the electrons released in bone and marrow differ. This will occur because of different electron binding energies and probabilities of Auger electron emission in the two neighboring media. Howarth (1965) took details of the electron emission spectra carefully into account in his calculations.

Values of $\overline{\overline{G}}$ are available for spherical and cylindrical cavities (Charlton and Cormack, 1962; Aspin and Johns, 1963; Howarth, 1965; Charlton, 1970; Unnikrishnan, 1977). The marrow cavities of trabecular bone are, however, very irregular in shape and size. For these, analytical calculations using Eq. (16) seem impossible. To solve this problem, Whitwell and Spiers (1976) took another approach to calculate the geometric factor $\overline{\overline{G}}$ based on a Monte Carlo method. Measured "omnidirectional" distributions of the chord lengths through the lamellae and marrow cavities of human trabecular bones (Beddoe *et al.*, 1976; Beddoe, 1977) were used to generate a series of random passages of electrons through varying thicknesses of bone and marrow. The approach of assuming straight-line electron paths was still used and the energy imparted along the path was calculated by means of a relationship between range (R) and energy (E), $R = AE^m$, where A and m are adjustable parameters. The mean absorbed dose in bone marrow could then be deduced from the distribution of cavity chord lengths and the mean value for the energy imparted along a chord of given length, derived in the Monte Carlo calculations.

While Whitwell and Spiers (1976) calculated the mean absorbed dose in bone marrow from β emitters incorporated within the bone, King and Spiers (1985) adapted the results to the case of photon irradiations in the energy range 30–140 keV. They present their results as "the fractional photoelectron dose increment." With the notation used in this chapter, their expression for this quantity is

$$[\overline{D}_m]_{PE}/K_{c,m} = [(\tau_{en}/\rho)_b(\overline{S/\rho})_b^m - (\tau_{en}/\rho)_m]\overline{\overline{G}}/(\mu_{en}/\rho)_m \qquad (17)$$

This photoelectron dose increment is due to the increased release of photoelectrons in bone compared to bone marrow; τ_{en}/ρ is the photoelectric component of the mass energy absorption coefficient μ_{en}/ρ, and $(\overline{S/\rho})_b^m$ is a weighted average of the ratio of the electron mass stopping power in marrow to that in bone.

King and Spiers (1985) derived the expression in Eq. (17) from first principles without any reference to the old theory. It may be interesting to find the physical connection between the formulas of the new [Eq. (17)] and old [Eq. (16)] theories. From Eq. (16) one has, by substituting $(R_b\rho_b)/(R_m\rho_m)$ with $(\overline{S/\rho})_b^m$,

$$\frac{\overline{D}_m - K_{c,m}}{K_{c,m}} = \frac{K_{c,b}(\overline{S/\rho})_b^m - K_{c,m}}{K_{c,m}}\overline{\overline{G}} \qquad (18)$$

Now, $K_c = (\mu_{en}/\rho)\Psi$, where Ψ is the energy fluence of the photons. Ψ is assumed to be the same in the marrow cavity and in the surrounding bone (at least within one electron range from the interface). Furthermore, the mass energy absorption coefficient μ_{en}/ρ can be decomposed into its photoelectric and Compton scattering components: $\mu_{en}/\rho = \tau_{en}/\rho + \sigma_{en}/\rho$. By neglecting the Compton scattering components [or equating $(\sigma_{en}/\rho)_b(\overline{S/\rho})_b^m$ with $(\sigma_{en}/\rho)_m$], Eq. (17) is obtained. In their derivation of Eq. (17), King and Spiers (1985) assumed that the energy of the photon is completely transferred to the electron in a photoelectric interaction. In deriving Eq. (18) from Eq. (16) it was tacitly assumed that the value of $\overline{\overline{G}}$ in the two terms of Eq. (16) is identical, which will not be strictly true if the binding energies of the released electrons are taken into account.

The theoretical results of King and Spiers (1985) were compared to earlier calculations and to results of careful measurements using thermoluminescent LiF powder dispensed into the cavities of human bone specimens (Fig. 8). The percentage excess absorbed dose (Fig. 8) exhibits a maximum at about 50 keV. The maximum is due to the combined effect of an increasing relative probability of photoelectric absorption in bone and decreasing electron ranges with decreasing photon energy. The percentage excess absorbed dose varies with age and the bone considered. For the parietal and possibly other bones in the head, it may run from 30 to over 40% (King and Spiers, 1985).

In Monte Carlo calculations (Rosenstein, 1976; Drexler *et al.*, 1985a,b; Jones and Wall, 1985) of organ mean absorbed doses using a mathematical phantom, the skeleton is treated as a uniform medium (a mixture of bone and marrow). Calculation of the mean absorbed dose in the bone marrow (m) of the various parts of the skeleton is subsequently derived in two steps. (1) The mass integral of the bone marrow collision kerma $K_{c,m,i}$ in skeletal region i is derived from the energy imparted $\varepsilon_{s,i} = \int(\overline{\mu_{en}/\rho})_{s,i}\Psi_i\, dM$ to the assumed uniform skeleton medium (s) of that region:

$$\int_{M_{m,i}} K_{c,m,i}\, dM = \varepsilon_{s,i} f_{m,i} \frac{(\overline{\mu_{en}/\rho})_{m,i}}{(\overline{\mu_{en}/\rho})_{s,i}} \qquad (19)$$

where $f_{m,i}$ is the fraction by weight of marrow in region i and $M_{m,i}$ the marrow mass. (2) Equation (17) is applied to $\overline{K}_{c,m,i} = (1/M_{m,i})\int K_{c,m,i}\, dM$ to account for the excess absorbed dose from the photoelectrons liberated in bone.

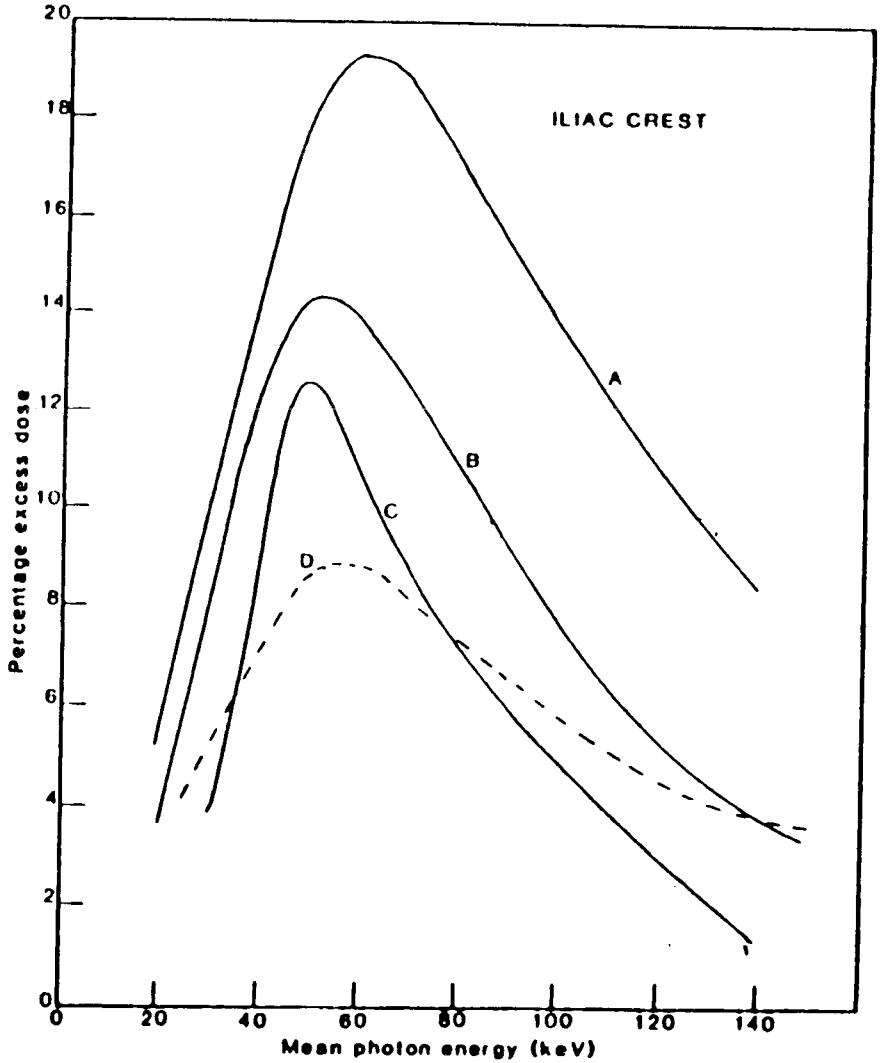

Fig. 8. Percentage excess absorbed dose (above $K_{c,m}$) to bone marrow of the iliac crest: (A) assuming cylindrical cavity shapes; (B) and (C) refined theoretical and experimental results, respectively; (D) assuming spherical cavity shapes. [From King and Spiers (1985).]

The choice of value for $(\mu_{en}/\rho)_m$ is not clear. The common use of the mass energy absorption coefficient for muscle must be questioned (King and Spiers, 1985). The considerable amount of fat in bone marrow [40% according to the ICRP Reference Man data (ICRP, 1975)] means that its chemical composition differs significantly from that of muscle (see also ICRU, 1989).

V. Energy Imparted to the Patient

The quantity mean energy imparted to the total body of a patient or to a specified volume can be determined from two different definitions (Alm Carlsson, 1985):

$$\bar{\varepsilon} = \bar{R}_{in} - \bar{R}_{out} + \overline{\Sigma Q} \tag{20}$$

and

$$\bar{\varepsilon} = \int_M D\, dM \tag{21}$$

R_{in} and R_{out} are the radiant energies incident on and escaping from the volume, D is the absorbed dose, and M is the mass of the volume. The bars indicate expectation values. As no changes in rest mass energy of nuclei or elementary particles occur with the photon energies used for diagnostic x-ray examinations, $\overline{\Sigma Q}$ occurring in the first definition is omitted in the following.

Equation (20) can be solved if the vectorial energy fluence Ψ over the surface of the object is known, e.g.,

$$\bar{\varepsilon} = -\oiint_{S(V)} \Psi \cdot d\mathbf{A} \tag{22}$$

where $S(V)$ is the surface area of the volume V, and dA is an element of $S(V)$ with its area vector $d\mathbf{A}$ pointing out of the volume (Alm Carlsson, 1985). In x-ray diagnostics the directions of the incident radiation are easy to determine, which simplifies the determination as described in Section V,A.

Equation (21) can be solved by determining the spatial distribution of absorbed dose in the volume. When only a small part of the volume or body is irradiated, Eq. (21) can, in some cases, be solved in a simplified way (Section V,B).

A. Determination of $\bar{\varepsilon} = \bar{R}_{in} - \bar{R}_{out}$

Equation (20) may be written

$$\bar{\varepsilon} = \bar{R}_{in} - \bar{R}_{out} = \bar{R}_{in}\frac{\bar{R}_{in} - \bar{R}_{out}}{\bar{R}_{in}} = \bar{R}_{in}\mathrm{IF} \tag{23}$$

where IF stands for *imparted fraction*. For the determination of $\bar{\varepsilon}$, $\bar{R}_{in}$ and IF are deduced separately.

1. *Determination of Imparted Fraction, IF*

Early investigations simply neglected the escape of primary and secondary radiations and took IF = 1 (Bjärngard *et al.*, 1960; Reinsma, 1962;

van Aken and van der Linden, 1966; Jensen, 1984). Later, imparted fractions were derived, preferably by Monte Carlo calculations (Dance, 1980; Doi and Chan, 1980; Shrimpton *et al.*, 1984; Persliden and Alm Carlsson, 1984). The imparted fraction for an incident pencil beam of photons (zero field area) varies with photon energy, beam direction, beam position, and thickness, shape, and composition of the phantom. From such calculations it is possible to deduce the imparted fraction for representative x-ray examinations by integrating over energy, field area, etc.

Persliden and Alm Carlsson (1984) used laterally infinite 10–300-mm-thick water slabs and monoenergetic photons with energies from 5 to 300 keV as well as realistic energy spectra. Alm Carlsson *et al.* (1984) extended the calculations to parallelepipeds of sizes simulating different patients or parts of the body. The influences of photon energy, field size, and focal distance on the imparted fraction were illuminated in detail.

Shrimpton *et al.* (1984) calculated imparted fractions for irradiations of the adult trunk and head. They defined their imparted fraction IF_t slightly differently from that in Eq. (23), namely as the fraction of the radiant energy in the total beam that is imparted to the patient. Thus, if a is the fraction of the beam used (i.e., hitting the patient), the fraction $1 - a$ (for which IF = 0) passes outside the body. The fraction $1 - a$ is estimated to be 37% in skull examinations. For different acceleration voltages, Shrimpton *et al.* give a range of values for IF_t corresponding to variations in beam filtration, beam size, and position of the entrance field. Their values for the trunk (simulated by a water box) are within ±10% of the mean, the range of values being due mainly to variations in field size and beam position. Those for the head (simulated with a water phantom containing simple bone structures) are within ±3% of the mean, depending on beam filtration and the view (AP/PA or LAT). In this case there is no dependence on field size since all of the head is irradiated and the field size is constant.

In measurements of energy imparted using a transmission chamber (Section V,A,4), the first step is to determine the incident radiant energy of the total beam, $R_{in,t}$. Equation (23) can be solved either by using $R_{in,t}$ as the incident radiant energy and adding the radiant energy passing outside the patient to R_{out}, as in Eq. (24) (Shrimpton *et al.*, (1984), or, as in Eq. (25), by regarding $aR_{in,t}$ as the incident radiant energy (Jones and Wall, 1985).

$$\bar{\varepsilon} = \bar{R}_{in,t}IF_t = \bar{R}_{in,t}\frac{\bar{R}_{in,t} - (1 - a)\bar{R}_{in,t} - \bar{R}_{out}}{\bar{R}_{in,t}} \tag{24}$$

$$\bar{\varepsilon} = a\bar{R}_{in,t}IF = a\bar{R}_{in,t}\frac{a\bar{R}_{in,t} - \bar{R}_{out}}{a\bar{R}_{in,t}} \tag{25}$$

When using imparted fractions from the literature, it is important to combine them with the correct value of the incident radiant energy ($R_{in,t}$ or $aR_{in,t}$).

Besides organ mean absorbed doses, Jones and Wall (1985) calculated imparted fractions for the various views (AP, PA, LAT, OBL) and typical values for the fraction a of 12 common x-ray diagnostic examinations using a mathematical phantom (containing all relevant organs) and a range of beam qualities. Figure 9 presents the range of values of IF from their calculations, assuming that all of the beam hits the patient ($a = 1$).

The values of IF derived for a 150-mm-thick, laterally infinite water slab by Alm Carlsson *et al.* (1984) compare well in Fig. 9 with those derived for the more sophisticated body phantom. For the skull irradiations, this good agreement seems fortuitous. With respect to the trunk irradiations, the lateral escape of radiant energy from a finite water box, simulating the adult trunk (200 mm thick, 300 mm wide, and 1 m long), is

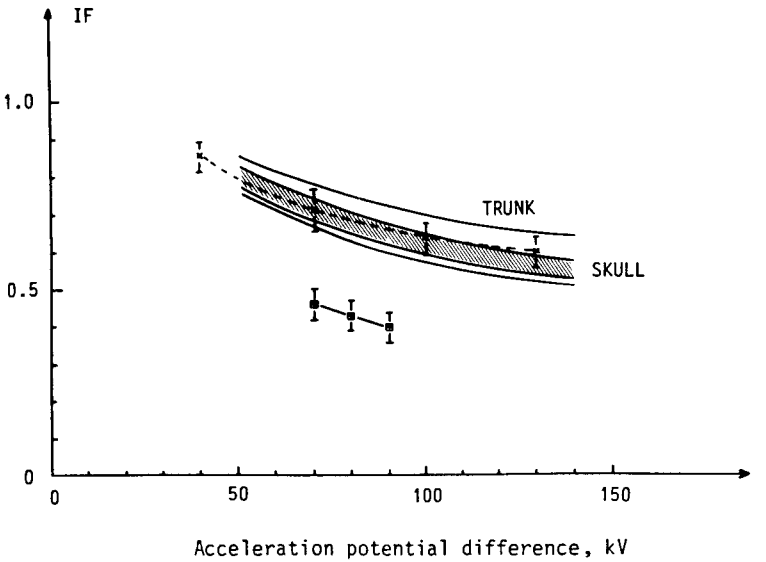

Fig. 9. Ranges of IF values in irradiations of the trunk and entire skull (shaded area), derived using Monte Carlo calculations and a mathematical (adult) phantom in simulating 12 common roentgen examinations (Jones and Wall, 1985). The variation in IF for each acceleration potential difference is due to variations in beam geometry and beam filtering. Values of IF are also given for (×) 150-mm-thick, laterally infinite water slab with indicated ranges due to an extreme variation in beam filtering (Alm Carlsson *et al.*, 1984) and (■) periapical dental radiography (long cone paralleling technique, rectangular collimation to film size) derived for a female patient with indicated ranges due to variations in projection only (S. J. Gibbs, personal communication, 1988).

well approximated by considering a thinner, laterally infinite slab. The same slab (150 mm) is a good approximation for both the LAT and AP/PA views. The relatively larger lateral escape in the LAT view is (more than) compensated by the larger thickness (300 mm as compared to 200 mm in the AP/PA view) and, consequently, smaller transmitted fraction in this geometry. The IF values of Shrimpton *et al.* (1984) are also in good agreement with those in Fig. 9, especially for the skull.

Typically, the higher IF values for the trunk irradiations in Fig. 9 are for an examination at the center of the trunk with the entrance field well within the edges of the phantom (e.g., examination of the kidneys). The lowest values are for an examination at a corner of the phantom (e.g., the shoulder) with high probabilities of escape of radiant energy.

S. J. Gibbs (personal communication, 1988, from Gibbs *et al.*, 1984) derived values of IF applicable to the irradiation geometries of dental intraoral examinations. The calculations refer to the anatomy derived from CT scans of a female cadaver (Pujol and Gibbs, 1982). The comparatively low values of the IF (Fig. 9) may be attributed to the thin body region radiographed. The energy imparted to the intraoral film package, simulated in the calculations, has been subtracted in deriving the IF shown in Fig. 9. Using a short-cone, bisecting-angle technique and a circular beam of 7-cm diameter, the imparted fractions IF are 5–10% higher, due to less shielding by the film package.

2. *Determination of Incident Radiant Energy, R_{in}*

The radiant energy in the total beam incident on the patient in an x-ray diagnostic examination can be recorded and derived using a thin, flat ionization chamber (monitor), perpendicular to the beam axis, that measures the air collision kerma $K_{c,air}$ integrated over the beam area A, $\int_A K_{c,air}\, dA$ (Airth, 1959, 1964; Carlsson and Lidén, 1959; Neboschew and Schott, 1959; Reinsma, 1959, 1962; Goldman *et al.*, 1960; Zieler, 1960; Arnal and Pychlau, 1962; Morgan, 1961; Pychlau and Pychlau, 1964; Carlsson 1965a). With

$$K_{c,air} = \int_0^\infty \left(\frac{\mu_{en}}{\rho}\right)_{air} \Psi_{h\nu}\, d(h\nu) = \left(\overline{\frac{\mu_{en}}{\rho}}\right)_{air} \Psi \tag{26}$$

$R_{in,t}$ can then be written

$$\begin{aligned} R_{in,t} &= \int_A \Psi \cos\theta\, dA = \int_A \frac{K_{c,air}}{\overline{(\mu_{en}/\rho)_{air}}} \cos\theta\, dA \\ &= \frac{1}{\overline{\overline{(\mu_{en}/\rho)_{air}}}} \int_A K_{c,air} \cos\theta\, dA = \frac{\overline{\cos\theta}}{\overline{\overline{(\mu_{en}/\rho)_{air}}}} \int_A K_{c,air}\, dA \end{aligned} \tag{27}$$

where $\overline{\overline{(\mu_{en}/\rho)_{air}}}$ is averaged over both photon energies and beam area, and θ is the angle of incidence to the normal of the area element dA. Usually, the approximation $\cos\theta \simeq 1$ can be used.

3. *Converting $\int_A K_{c,air}\, dA$ to Energy Imparted, ε*

As mentioned above and discussed in detail in the next section, $\int_A K_{c,air}\, dA$ can be measured. Equations (25) and (27) give

$$\frac{\varepsilon}{\int_A K_{c,air}\, dA} = a\ \mathrm{IF}\ \frac{\overline{\cos\theta}}{\overline{\overline{(\mu_{en}/\rho)_{air}}}} \simeq \frac{a\ \mathrm{IF}}{\overline{(\mu_{en}/\rho)_{air}}} \tag{28}$$

This is the quantity that, for a given primary spectrum, phantom size and shape, field area, and position, converts the measured value $\int_A K_{c,air}\, dA$ to energy imparted to the patient. In the last (approximate) equality, the averaging of $\overline{(\mu_{en}/\rho)_{air}}$ over beam area is neglected, and $\cos\theta \simeq 1$ is used.

While values of imparted fractions IF (Fig. 9) are not very sensitive to the beam filtration for a given acceleration voltage, values of $R_{in,t}$ [Eq. (27)], and consequently of the conversion factor $\varepsilon/\int_A K_{c,air}\, dA$ [Eq. (28)], are. This is due to the strong energy dependence of $(\mu_{en}/\rho)_{air}$.

a. Averaging $(\mu_{en}/\rho)_{air}$. Tabulated fluence energy spectra (Birch *et al.*, 1979; Reiss and Steinle, 1973) are presented for a given acceleration voltage (constant or with a given ripple), anode angle, and total filtration. Apparently, specification of total filtration is not sufficient for a unique presentation of the energy spectrum. In comparing values of $\overline{(\mu_{en}/\rho)_{air}}$ to be used in Eqs. (27) and (28), as derived by Shrimpton *et al.* (1984) using spectra of Birch *et al.*, and by Alm Carlsson *et al.* (1984) using spectra of Reiss and Steinle, differences as great as 30% occur at the same (constant) voltage and total filtration (anode angles 17° and 15°, respectively). This can be explained by the problems in defining inherent filtration (Section III,C). However, the values of $\overline{(\mu_{en}/\rho)_{air}}$ coincide when compared on the basis of acceleration voltage and HVT values. This is the reason for representing conversion factors as a function of HVT in Fig. 10. In Fig. 10, values of the conversion factor $\varepsilon/\int_A K_{c,air}\, dA$ for the trunk and head have been derived using the IF values of Jones and Wall (1985) in Fig. 9 and values of $\overline{(\mu_{en}/\rho)_{air}}$ averaged over the constant potential energy spectra by Birch *et al.* (1979) (17° W anode), and presupposing that all of the beam hits the patient [$a = 1$ in Eq. (28)].

The spread in the values for each HVT and acceleration voltage (Fig. 10) is due to the variations in field size and field position which occur in the 12 x-ray examinations considered by Jones and Wall (1985). The

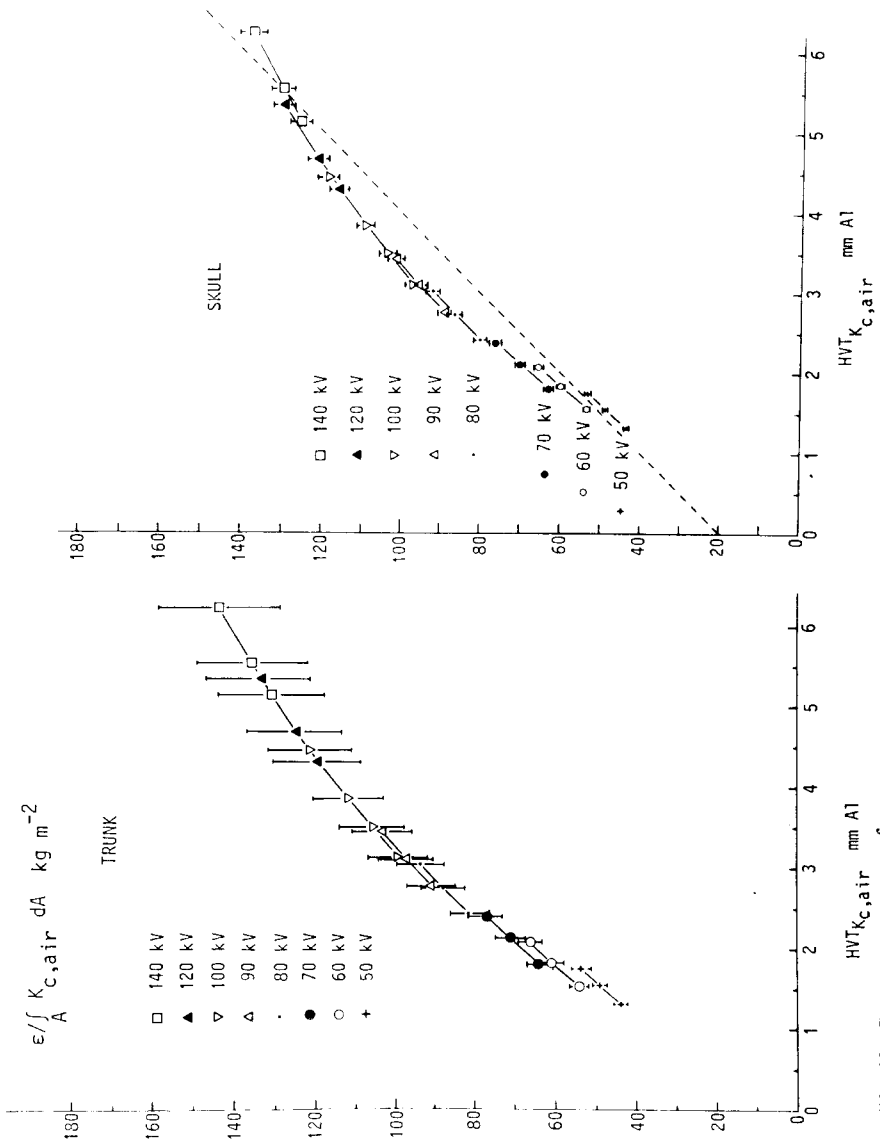

Fig. 10. Conversion factor $\varepsilon/\int_A K_{c,air}\, dA$ as a function of the half-value thickness (HVT) with the acceleration voltage as parameter for examinations of the adult trunk (left) and the adult skull (right). The values were derived using IF values from Jones and Wall (1985) and constant-potential-energy spectra from Birch *et al.* (1979). It is assumed that all of the beam hits the patient [$a = 1$ in Eq. (28)]. The dashed, straight-line approximation (right) was used by Stenström *et al.* (1988) for acceleration voltages ≤70 kV and intraoral radiography.

spread is greater the higher the HVT due to increasing probability of lateral escape of radiant energy with increasing incident photon energy. One also notices that for HVT values above 3.5-mm Al, the HVT is sufficient for specifying beam quality with respect to the conversion factor. The dashed line in Fig. 10b gives the straight-line approximation of the conversion factor used by Stenström *et al.* (1988) for estimating energy imparted to the patient in dental radiography.

For accurate use of the conversion factors in Fig. 10, HVT measurements should be performed. Such measurements are rather time consuming. With access to a Compton spectrometer (Matscheko and Ribberfors, 1987; Matscheko, 1988), a complete energy fluence spectrum can be determined with the same effort and tube loading. A direct measurement of the energy spectrum allows accurate determination of $(\overline{\mu_{en}/\rho})_{air}$ for the particular x-ray unit and working conditions (milliamperes).

b. Conversion Factors in Practical Use. Conversion factors reported by Pychlau and Bunde (1965) showed a constant value of $\varepsilon/\int_A K_{c,air}\, dA$, independent of beam quality. This is an attractive feature, and their conversion factors are still in use. However, it has been shown that the constancy of the conversion factor was caused by erroneous use of the concept of effective energy (Alm Carlsson and Carlsson, 1984) in deriving $R_{in,t}$ from Eq. (27). Pychlau and Bunde determined R_{out} [Eq. (23)] correctly from a sophisticated experiment using a thick NaI spectrometer placed at more than 400 points around a man-shaped phantom.

The conversion factors derived by Alm Carlsson *et al.* (1984) for a 15-cm-thick, laterally infinite water slab agree well with the midrange values in Fig. 10. This is also the case for those of Carlsson (1963), derived for a 20-cm water slab (see Fig. 33). The possibility of changing the spectral response of the monitor to follow the conversion factor has been discussed by Reinsma (1962) and Carlsson (1965a).

4. *Measurement of* $\int_A K_{c,air}\, dA$

The air collision kerma $K_{c,air}$, integrated over the beam cross-sectional area perpendicular to the beam axis, is measured (Fig. 11) with a plane-parallel ionization chamber (monitor) having an area larger than the largest beam cross section. The monitor measures $\int_A K_{c,air}\, dA$ independent of the divergence of the x rays, as long as it can be regarded as thin compared to the mean free paths of the photons (Alm Carlsson and Carlsson, 1982).

a. Calibration of the Monitor. $\int_A K_{c,air}\, dA$ does not change with distance from focus as long as attenuation in air can be neglected. An ioniza-

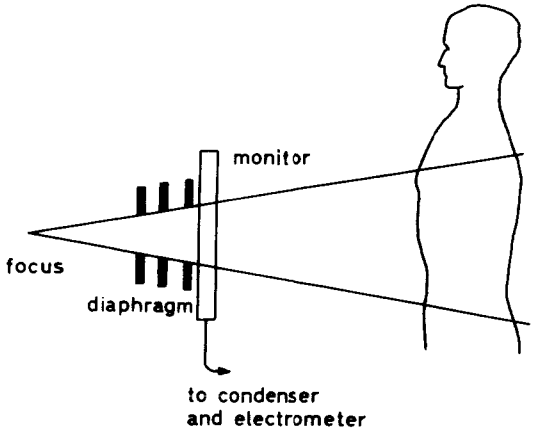

Fig. 11. Schematic drawing showing the measuring principle. [From Carlsson, 1965a).]

tion chamber, calibrated to measure $K_{c,air}$, can then be placed in the beam, under reasonably scatter-free conditions, on the patient's side of the monitor (Fig. 11). The monitor can be calibrated to measure $\int_A K_{c,air}\, dA$ by introducing an extra collimator with well-determined area on the focal side of the monitor and correcting the collimator area to the area A at the distance where $K_{c,air}$ is determined. A necessary condition is that the air collision kerma is constant over the area A. In order to get a large signal from the monitor, it is tempting to use a large field area. For careful calibration of his monitors, Carlsson (1965a) mapped out, in a few cases, the distribution of air collision kerma in a plane as shown in Fig. 12. These measurements were extended outside the nominal field contours to include effects of penumbra and extrafocal radiation. Shrimpton and Wall (1982) determined the field area by using the limits of 50% optical density on an x-ray film. They found, with moderate field areas, the exposure at the center of the field to be a reasonable estimate of the exposure averaged over the entire field.

b. Heel Effect. The field of primary photons varies over the beam cross section in both magnitude and quality (spectral distribution). This is an effect (the heel effect) of the angle between the anode plate and the central ray. Figure 12 shows how the air collision kerma of the primary photons varies over field area for an anode angle of 17.5° (Carlsson, 1965a). In modern x-ray tubes, with anode angles of 7°–11°, the heel effect is more pronounced.

The energy distribution of the primary photons depends on the emission angle from the anode and thus varies over the field area. The degree

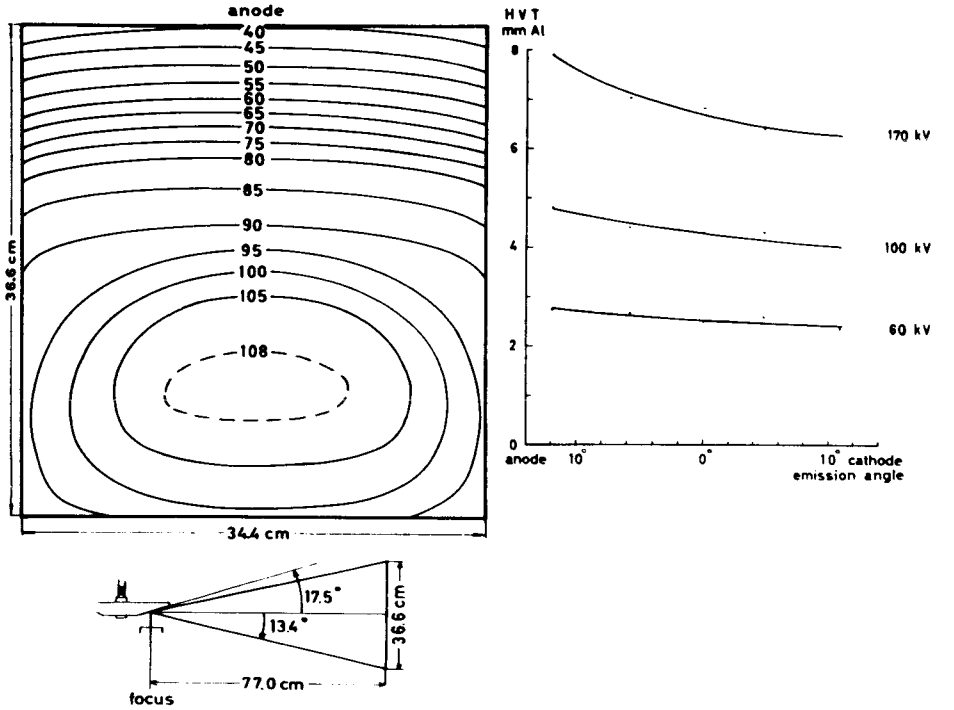

Fig. 12. (Left) Measured values of $K_{c,air}$ from a diagnostic x-ray tube at 75 kV and HVT = 4.3 mm Al. (Right) Variation of $HVT_{K_{c,air}}$ with emission angle from the x-ray tube. [From Carlsson (1963).]

of variation is illustrated in Fig. 13, which shows energy distributions measured by Svahn (1977) in various directions from a 95% tungsten and 5% rhenium anode. The variation of HVT with emission angle is illustrated in Fig. 12.

If the variation of $K_{c,air}$ over beam area is neglected and $K_{c,air}$ at the central ray is assumed to be valid at all points of the field, $\int_A K_{c,air}\, dA$ will be overestimated by about 18% for the case in Fig. 12. With modern tubes, having anode angles about 11° instead of 17°–18°, the overestimate can amount to 40% if a very large field area is used at the calibration.

c. Tabletop. Figure 14 shows how the calibration value of a monitor varies with HVT for some x-ray tubes, with and without a tabletop between the monitor and the calibrated ionization chamber (patient). The low calibration values at low HVT are due to attenuation in the walls of the monitor and in the tabletop. The values presented as continuous

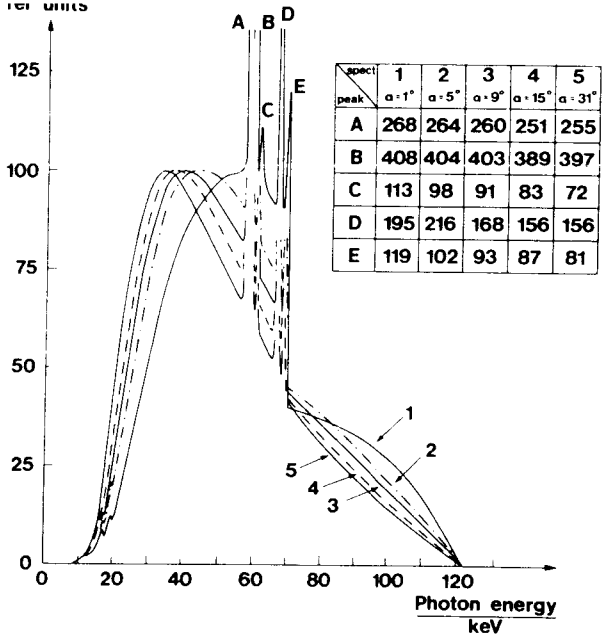

peak \ spect	1 α=1°	2 α=5°	3 α=9°	4 α=15°	5 α=31°
A	268	264	260	251	255
B	408	404	403	389	397
C	113	98	91	83	72
D	195	216	168	156	156
E	119	102	93	87	81

Fig. 13. Fluence spectra, differential in energy $\phi_{h\nu}$, obtained at 120 kV in different directions (α) of emission relative to the anode surface. The central ray corresponds to $\alpha = 15°$. The peaks of the characteristic radiation are not fully illustrated but the relative values of the photon fluence rate of the peaks, including the continuous distribution, are given in the table. [From Svahn (1977).]

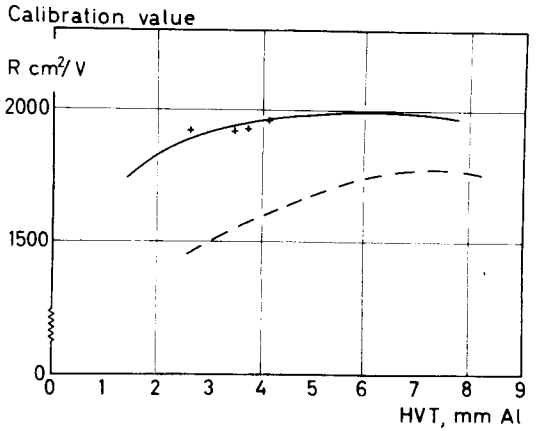

Fig. 14. Calibration values, in units of roentgens centimeters squared per volt, of a monitor as a function of HVT (———) without and (····) with a couch (table top) between monitor and patient. The crosses show calibration values determined using a large field and isoexposure curves, as in Fig. 12. [From Carlsson (1965a).]

curves are obtained with a small field area (≈100 cm² at a focal distance of 1 m). The crosses are results from determination of $\int_A K_{c,air}\, dA$ by isoexposure measurements as in Fig. 12.

d. Backscatter Problems. The monitor is sensitive to backscatter from the patient. This is generally no problem with overcouch tubes but must sometimes be corrected for with undercouch tubes (Fig. 15).

e. Several Monitors in Parallel. Carlsson (1965a) had monitors on all x-ray tubes in the examination room with one to four monitors connected in parallel to one electrometer. The length of coaxial cables varied between 6 and 50 m. The ionization current charged a large (0.5 μF) condenser, whose voltage was measured by the electrometer. The total capacity of monitors and cables was less than 1% of that of the condenser; hence the influence of varying capacity on the calibration factors could be neglected.

f. Varying Calibration Factor During an Examination. The different calibration values for over- and undercouch tubes (Fig. 14) indicate that

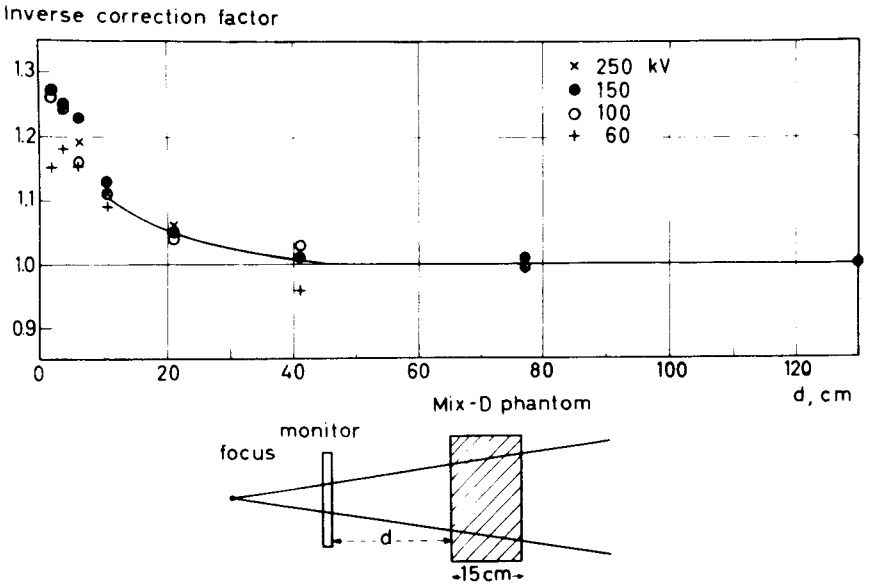

Fig. 15. Relative overestimate of the energy imparted, due to scattered radiation from the patient (detected by the monitor), as a function of the distance between monitor and patient. [From Carlsson (1965a).]

the signals from the different monitors must be separated (Shrimpton and Wall, 1982; Carlsson, 1965a). The conversion factor depends on the acceleration voltage and beam filtration (HVT) (Fig. 10). In many diagnostic examinations, the acceleration potential and the x-ray tubes are changed during the examination. Thus, signals obtained with different voltages must also be separated. Carlsson (1965a,b) solved this problem by connecting the monitors to a condenser and recording the potential as a function of time (Fig. 16). For all examinations, exposure data and a diagram as in Fig. 16 were recorded and the energy imparted from each part of the examination was calculated. Shrimpton *et al.* (1984) avoided this tedious work by determining an average conversion factor for each type of examination.

B. Determination of $\bar{\varepsilon} = \int_M D\, dM$ to Phantoms

The energy imparted to a body can, in principle, be measured by a tissue-equivalent chemical dosimeter filling a phantom, or by a water calorimeter. These dosimeters are, however, far too insensitive for use with diagnostic x-ray tubes.

Boag (1945) used a man-shaped phantom, the "celluloid man." This consisted of several plane-parallel ionization chambers in which the electrodes also functioned as phantom material. This phantom was used by Bewley *et al.* (1959) for determination of energy imparted from 200-kV and 8-MV x rays.

1. *Packing the Phantom with Dosimeters*

Mayneord and Clarkson (1944) used ionization chambers in a phantom and the equation

$$\bar{\varepsilon} = \int_M D\, dM \simeq \sum_{i=1}^{N} D_i\, \Delta M_i \qquad (29)$$

to determine the energy imparted. The method has become easier to apply with the introduction of TL dosimeters (Stenström *et al.*, 1986a). The dosimeters must be placed both within and outside the primary beam. In rotational, panoramic views of the teeth, a scanning fan beam moves so that thin, line-shaped dose maxima are created in the head, making application of Eq. (29) especially difficult.

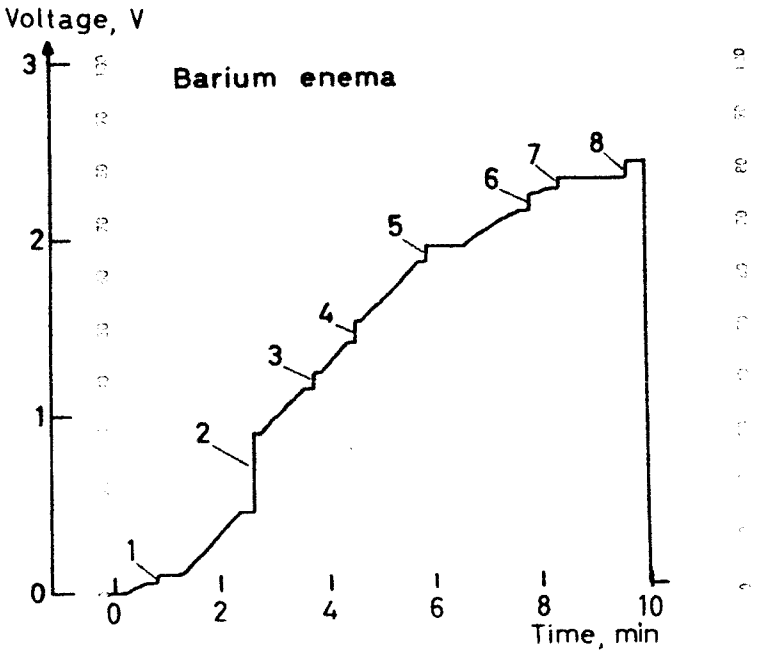

Fig. 16. Record of a colon examination with mixed fluoroscopy and radiography. The exposure data are given below. [From Carlsson (1965b).]

No.	kV	mAs	Film dimension (cm^2)	Position of patient	Roentgen tube	Energy imparted (mJ)
1	120	20	24 × 30	Supine	Undercouch	12
2	120	160	24 × 30	Lateral	Undercouch	107
3	120	40	24 × 30	Oblique	Undercouch	22
4	120	40	24 × 30	Oblique	Undercouch	29
5	120	32	24 × 30	Slight oblique	Undercouch	23
6	120	32	24 × 30	Slight oblique	Undercouch	22
7	120	25	18 × 24	Slight oblique	Undercouch	14
8	170	6	30 × 40	Prone	Overcouch	28
Fluoroscopy	90	600	—	Varying	Undercouch	250
					Sum	507

Huda and Sandison (1984) used an anthropomorphic (Rando) phantom, packed with TL dosimeters, to derive mean absorbed doses in various body organs. The method was used by Huda (1984) for determination of mean organ absorbed doses and energy imparted to the total body in CT examinations.

2. *Use of Central-Axis Depth–Dose Curves*

Under conditions discussed below, the energy imparted may be approximated:

$$\bar{\varepsilon} = \int_M D\, dM \simeq \rho A_0 \int_0^L D(x) \left(\frac{F + x}{F}\right)^2 dx \qquad (30)$$

where ρ is the density, A_0 the field area at the surface, F the focus-to-surface distance, L the thickness of phantom, and $D(x)$ the absorbed dose on the central axis at depth x in the phantom.

The integration in Eq. (30) extends over the volume defined by the primary beam. Since central-axis depth doses $D(x)$ are used, it is clear that Eq. (30) overestimates the energy imparted to the volume within the nominal beam. This will, more or less accurately, compensate for the contribution to the energy imparted by scattered radiation in the volume outside the primary beam [not included in the integration, Eq. (30)]. If the central-axis depth doses used in Eq. (30) are obtained with a very large field, to yield conditions of saturated scatter at the central axis, the compensation will be exact for a body extending far beyond the primary beam (Happey, 1940, 1941). This "saturated-scatter method" thus requires use of depth doses obtained with a large field rather than those associated with the actual field A_0. Otherwise, Eq. (30) will heavily underestimate $\bar{\varepsilon}$ for small fields since the contribution to the energy imparted to the body by scattered photons escaping the primarily irradiated volume will be largely neglected.

Carlsson (1963) corrected saturated-scatter depth doses, obtained with a thick phantom, for the loss of backscattered photons before the data were applied to thinner phantoms.

Harrison (1981, 1982, 1983), on the basis of extensive measurements of depth doses for diagnostic x rays, has applied the saturated-scatter method to calculate the energy imparted to the patient. To account for the lateral escape of radiant energy from a finite-sized patient, he suggested use of depth doses for a 30×30 cm^2 field to derive the energy imparted to adult patients and a 20×20 cm^2 field in pediatric examinations. Conversion factors $\varepsilon / \int_A K_{c,air}\, dA$, derived by Harrison (1983) for the adult patient (calculated with depth doses for a 30×30 cm^2 field to a depth of 20 cm), tend to overestimate the true values (Shrimpton and Wall, 1983), being 5–15% above the midrange values in Fig. 10a.

3. *Determination of Energy Imparted from X-Ray Examinations with Standardized Field Areas*

When field areas are standardized, the monitor chamber is unnecessary. Instead, the quantity $\int_A K_{c,air}\, dA$ can be determined for all the technical factors used (field area, voltage, and tube charge). Conversion factors $\varepsilon / \int_A K_{c,air}\, dA$ can then be used as described above. Examinations allowing such simplified performance can be found in dental radiography, mammography, and computerized tomography.

VI. Determination of Organ Mean Absorbed Doses

With such low absorbed doses as the patients receive from x-ray examinations, only stochastic radiation effects are in general possible. In extreme cases, however, the risk of nonstochastic injury to the eye lenses cannot be neglected. For estimates of stochastic risk, the average absorbed dose in each radiosensitive organ is assumed to be the relevant quantity (Mayneord and Clarke, 1975; ICRP, 1977a). With small, sensitive dosimeters, it is possible to determine the absorbed dose at a position on or in the body from a single examination. In cases where the organ of interest is small and situated near the dosimeter, only small corrections are necessary (see below). Average absorbed doses in large or distributed organs inside the body must be determined in phantoms, either experimentally or by calculations. A general disadvantage with dosimeters on or in the patient is that their application disturbs the examination and their appearance in the image may disturb the diagnosis.

Bengtsson *et al.* (1978) determined the detriment to the Swedish population from induction of fatal cancer and severe genetic injury by diagnostic radiology. Their determinations are based on extensive measurements with thermoluminescent LiF dosimeters on the patient and in some cases in the rectum, as well as on measurements of energy imparted. Sometimes, detailed calculations for determination of the mean absorbed doses in different organs from the measurements were performed, but more often simplifying approximations were used. They estimated an accuracy of about ±10% in the physical measurements and about ±20% in determination of absorbed doses in the thyroid and testes from nearby dosimeters, as averaged over several patients. The mean absorbed doses in other organs (breasts, lungs, bone marrow, and ovaries) could have an uncertainty of about a factor of 2, as an average over several patients. In individual patients the uncertainty may be still higher.

A. Measurements

1. *Choice of Dosimeters*

For measurements on or in patients, two types of dosimeters predominate: ionization chambers and thermoluminescent materials.

a. Ionization Chambers. Air-filled ionization chambers with reasonably air-equivalent walls have the advantage of being nearly tissue equivalent in energy absorption properties over a wide range of photon energies. Their sensitivity (signal per unit air collision kerma) is proportional to the air volume. Large chambers, required for measurements of low absorbed doses, have several disadvantages. They overestimate the absorbed dose at a point within a body (Lidén, 1961; Harrison, 1981) (Section II). The translation of the dosimeter reading to average absorbed dose in a small organ (eye lens) may be problematic. The dosimeters easily disturb the image.

Using an ion chamber connected by cable to an electrometer and the polarizing voltage (Bjärngard *et al.*, 1959) has the advantages of high dynamic range (compared to condenser chambers), possibility of separating the contributions from different parts of the examination, and no wait for the results. Disadvantages are clumsiness and serious disturbances of the image when applied on a patient and within the radiation field.

A simple two-electrode condenser ionization chamber is electrically charged before and gradually discharged during the irradiation. The precision of this dosimeter is highest when about half of the charge has been neutralized. As the voltage approaches lower values, ionic recombination may become a problem. This means that the useful dose range is small.

Interesting variants of condenser chambers are two types of three-electrode chambers. One (Sievert and Walstam, 1951; Walstam, 1965) consists of three concentric tubes of graphite-coated paper insulated from each other. They form two ionization chambers, one inside the other. The volumes are adjusted so that the outer chamber is 10 times more sensitive than the inner one. An ionization chamber by Cederlund (1960) combines some of the advantages of the cable-connected and condenser chambers. This chamber has the usual central electrode. The other two electrodes are on the inside and the outside of the wall, which is made of an insulating material. Before use, a polarizing voltage is applied to the inner-wall electrode with the outer and central electrodes grounded. Large absorbed doses are measured by the decrease of the polarizing voltage to ground. Small doses can be measured with the same high sensitivity as by cable-connected chambers, using the potential difference of the central electrode and ground. This chamber has a useful range of 50 μGy to 40 mGy.

b. Thermoluminescence Dosimeters. In recent years, thermoluminescence dosimetry has been the method of choice for measurement of organ absorbed doses. The method is thoroughly described in the literature (Cameron *et al.*, 1968; McKinlay, 1981; Horowitz, 1984). The dosimeters can be used as powder, differently shaped pellets, rods, or foils. They are cheap, can be read out automatically, and can be used over a large dose range. Different materials are available. $Li_2B_4O_7$ is most equivalent to soft tissue (Christensen *et al.*, 1982); see Fig. 3 in Section II. LiF is somewhat less soft-tissue equivalent but has a higher sensitivity. Other materials, such as those based on $CaSO_4$ or CaF_2, can be very sensitive but have an unfavorable atomic composition for determination of absorbed doses in soft tissues.

The fluctuations of the non-radiation-induced signals to a large extent determine the precision in measurements of small absorbed doses. Spanne (1979) studied methods for reducing these fluctuations and could measure absorbed doses as small as 0.6 μGy with a signal-to-noise ratio of 3 using dosimeters containing 24 mg of LiF. This means that most organ absorbed doses can be determined from examination of a single patient instead of integrating the signals from 10 or more patients or phantom irradiations.

2. *Corrections of Dosimeter Readings to Yield Organ Mean Absorbed Doses*

a. Eye Lens. Bergström *et al.* (1972) used dosimeters on the upper eyelids for determination of average absorbed dose in the lens. The distance between the dosimeter and the center of the lens was 8 to 9 mm. Phantom experiments showed negligible differences in absorbed doses at these two positions. Montanara *et al.* (1986) corrected their measured values on the eyelids with a factor that varied from 0.92 to 0.88 for spectra of 100 kV down to 65 kV, respectively, to obtain absorbed doses in the lenses.

b. Gonads. Absorbed doses in the male gonads may be measured with the dosimeter on the scrotum. For determination of the average absorbed dose in the testes, the absorbed dose at a depth of 1 cm seems appropriate and the absorbed dose value measured with the dosimeter on the scrotum can be used without corrections (Hammer-Jacobsen, 1963). Absorbed doses in the female gonads have most often been based on measurements in the rectum, sometimes in the vagina. Hammer-Jacobsen (1963) investigated the position of the ovaries, rectum, and vagina in cadavers and found that, on the average, the absorbed doses measured in

the rectum should be multiplied by the factor 2.0 for AP projections and 1.3 for lateral projections. Measurements in the vagina could be used without corrections in AP and PA projections. Larsson (1958) took into account that contrast medium in the bladder shielded the ion chamber in the rectum but not the ovaries.

c. Thyroid. The thyroid is, like the testes and eye lenses, an organ in which the mean absorbed dose can be determined with relatively high accuracy using only one or two dosimeters on the patient. For example, Bengtsson *et al.* (1978) applied a correction factor of 0.9, allowing for attenuation in about 1 cm of interposing tissue.

d. Breast. Bengtsson *et al.* (1978) placed dosimeters on the skin at a location representative of the main part of the breast tissue, usually about 10 cm from the midline of the body and near the fourth or fifth rib. A correction factor of 0.8 was applied to take account of the attenuation in the breast, corresponding to the average attenuation in 2.5 cm of tissue. In some examinations to derive the mean absorbed dose in both breasts from a dosimeter placed on one breast (stomach, gallbladder, chest), the correction factor was 0.6. In the chest examinations, the dosimeter was then placed on the breast which, in the lateral projection, was nearest to the roentgen tube. In examinations where the main contribution to the mean absorbed dose in the breast comes from scattered radiation generated by distant primary photons (small intestine, colon), no attenuation correction factor was applied and the uncertainty in the mean absorbed dose in the breast was judged to be about a factor of 2.

A special problem is to determine the mean absorbed dose in the breast in mammography. Since mammography may be used for screening of asymptomatic women, the dosimetry of the breast must be carefully considered. Mammography dosimetry is treated separately in Section VI,C.

e. Bone Dosimetry (Red Bone Marrow, Bone Surfaces). Red bone marrow and bone surfaces are among the specified organs given a weight factor w_T for calculation of the effective dose equivalent H_E (Table I). There are physical and biological problems in determining the mean absorbed dose. The physical problems are the different attenuation and scattering in bone compared to soft tissues, as well as the absorbed dose enhancement to marrow and to the osteogenic tissues lining the bone surfaces, discussed in Section IV.

To determine the mean absorbed dose in such extended organs it is necessary to know the distribution of active bone marrow or bone surfaces. This biological problem has been reviewed by Ellis (1961). Much information can also be obtained from ICRP (1975) and Ellis *et al.* (1975). Cristy (1981b) presented the distribution of active bone marrow in various bones as a function of age in humans. Russell *et al.* (1964, 1966) developed a method for calculating active bone marrow mass for various body sites. The bone marrow contents in different bones given in Fig. 17 and Table II are assumed to be valid for a 40-year-old, average human. By means of Fig. 17 and the data in Table II, the fraction of active bone marrow irradiated in an x-ray examination can be determined with reasonable accuracy.

Bengtsson *et al.* (1978) found that for many examinations of the trunk and head the mean absorbed dose in bone marrow could be derived from measurements of $\int_A K_{c,air}\, dA$ using a proportionality constant $k = 1.7$ Gy J^{-1} kg m^{-2}. This value was derived from data presented by Ellis *et al.* (1975) and presupposes a uniform distribution of bone marrow over a projected body area of 0.2 m^2 in the AP and PA projections. Only in a few types of examination was this value of k judged to be in error by more than a factor of 2. In lumbar spine examinations and in urography the values $k/2$ and $k/5$, respectively, were used.

For complex trunk examinations involving fluoroscopy, Contento *et al.* (1988) also used conversion factors (derived from the Monte Carlo calculations by Jones and Wall, 1985) relating $\int_A K_{c,air}\, dA$ to the mean absorbed dose $\bar{D}$ in bone and bone marrow. Significantly larger values of $\bar{D}/\int_A K_{c,air}\, dA$ had to be used for PA compared to AP projections. A rough guide to the proportion of each examination that was AP or PA was obtained from pairs of dosimeters on the front and back of the trunk.

B. Calculations

Mean absorbed doses in various organs and for various diagnostic x-ray procedures have been calculated using Monte Carlo techniques and mathematical phantoms (Rosenstein, 1976, 1982; Kereiakes and Rosenstein, 1980; Drexler *et al.*, 1985a,b; Jones and Wall, 1985). The mathematical MIRD phantom (Snyder *et al.*, 1969), originally defined for determination of the effective dose equivalent in radiation workers from intake of radioactive nuclei, was used by Rosenstein (1976, 1982). The phantom is bisexual, with both ovaries and testes but with no female breast. Rosenstein modified the phantom for females by adding breasts to its chest wall. The total weight of the phantom was 70 kg for males and 70.3 kg for females. Rosenstein's calculations were used by Laws and Rosenstein (1978) in deriving values of the somatic dose index for males and females from typical diagnostic x-ray examinations.

Drexler *et al.* (1985a,b) refined the MIRD phantom, defining separate phantoms of different dimensions for males and females. Values of organ

TABLE II

MASS OF ACTIVE BONE MARROW IN GRAMS IN EACH SPACE ELEMENT IN FIG. 17[a]

Cube no.	Skull vertex	←Craniad						Transverse	sections					Caudad→		Ischium; prox. femur		Cube total
	C	D	E	F	G	H	I	J	K	L	M	N	O	P	Q	R	S	
1[b]																		
2							1.10	0.99	1.18	0.59	0.14							4.00
3		2.49	1.24			0.76	1.86	2.95	1.96	0.90				14.41	7.63			34.20
4		4.97	6.22				0.83	2.48	4.32	2.56	1.31	0.95	0.96	9.78	36.19			70.55
5		2.49	1.24			0.76	1.86	2.95	1.96	0.90				14.41	7.63			34.20
6							1.10	0.99	1.18	0.59	0.14							4.00
7[b]																		
8						2.53										1.60		4.13
9						3.83	6.71	2.93	2.11	2.48	0.34			9.32	8.56	10.00	4.00	50.28
10	2.49	8.70	4.97	2.49		3.32	0.43				0.44	0.71	0.48	26.16	24.77	13.05	5.83	93.82
11	4.97	2.49		3.01	2.00	12.17	31.37	26.60	32.19	46.52	18.75	20.23	22.17	58.32	9.05			289.90
12	2.49	8.70	4.97	2.49		3.32	0.43				0.44	0.71	0.48	26.16	24.77	13.05	5.83	93.82
13						3.83	6.71	2.93	2.11	2.48	0.34			9.32	8.56	10.00	4.00	50.28
14						2.53										1.60		4.13
15						8.60	7.26											15.86
16						9.20	3.38	2.27	2.67	1.48	0.23			8.16	6.23			33.62
17	2.49	4.97	2.49	3.50		5.15	0.13			0.10					6.23	10.72	2.33	38.11
18	4.97		2.49	13.78	19.17	18.52	0.91				0.87	1.19				7.00	4.66	73.56
19	2.49	4.97	2.49	3.50		5.15	0.13			0.10					6.23	10.72	2.33	38.11
20						9.20	3.38	2.27	2.67	1.48	0.23			8.16	6.23			33.62
21						8.60	7.26											15.86
22[b]																		
23							0.06	0.51	0.85									1.42
24	1.24	4.97	1.24	3.32	0.74	0.04	0.62	0.42	0.24	0.15								12.98
25	2.49	4.97	2.49	1.23	1.23	7.70	6.32	5.85	3.51									35.79
26	1.24	4.97	1.24	3.32	0.74	0.04	0.62	0.42	0.24	0.15								12.98
27							0.06	0.51	0.85									1.42
28[b]																		
Section totals	24.87	54.69	31.08	36.64	23.88	105.25	82.53	55.07	58.04	60.48	23.23	23.79	24.09	184.20	152.08	77.74	28.98	Grand total: 1,046.64 g

[a] Source: Russell *et al.* (1964, 1966).
[b] No active bone marrow.

mean absorbed doses are given for a variety of diagnostic x-ray procedures and radiation qualities (kilovolts and beam filtrations). The values are normalized to the exposure free in air (without backscatter) on the central axis in the entrance field.

Jones and Wall (1985) produced extensive tables of organ mean absorbed doses from 11 common examinations, with clear indication of beam size and position on the phantom. The positions of the various organs within the primary field are also shown. A bisexual phantom including the female breast (assumed to consist of a 50 : 50 mixture by weight of fat and water) was used. In addition to the organ mean absorbed doses, values of imparted fractions (Fig. 9), easily obtained from the Monte Carlo calculations, and backscatter absorbed dose coefficients are

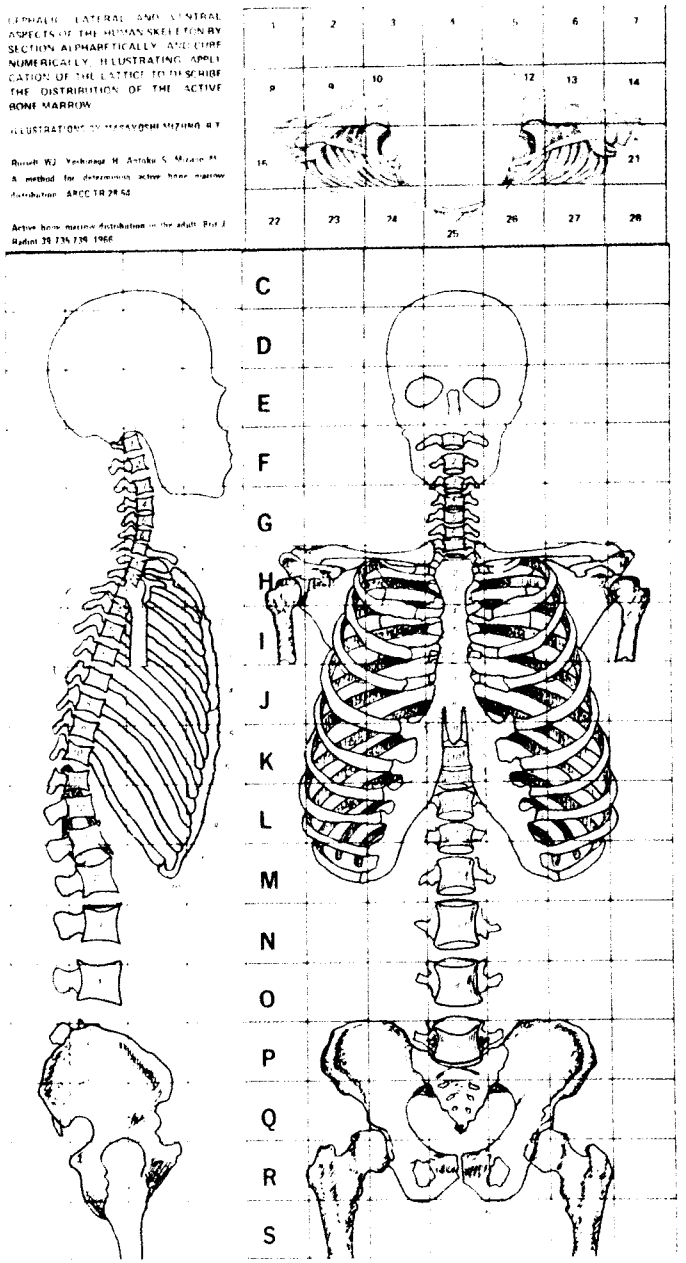

Fig. 17. Cubic space elements containing bones. [From Russell *et al.* (1964).]

given. The backscatter coefficients R, called "backscattered fraction" by Jones and Wall, can be used to derive the backscatter factor $B = 1 + R$, from which the absorbed dose under electronic-equilibrium conditions at the phantom surface can be derived from determination of the tissue collision kerma [derivable from measurements of air collision kerma, Eq. (5)] free in air at the entrance field (Carlsson and Lidén, 1968). Problems involved in determinations of the backscatter factor have been discussed by Grosswendt (1984) and Chan and Doi (1981).

In a large survey of the radiation burden to the British population, Shrimpton *et al.* (1986a) derived organ mean absorbed doses to individual patients from measurements of entrance skin absorbed doses and the Monte Carlo calculations of Jones and Wall (1985), which relate the various organ mean absorbed doses to each other.

The Monte Carlo calculations are generally derived for a standard phantom and standard field sizes and focus–skin distances. Thus, no information is provided about the influence on organ mean absorbed doses of variations in these parameters, including size of the patient. Patients also show variations in the relative positions of the organs. For deep-lying organs, these variations are also impossible to account for in direct measurements on the patients.

In Fig. 18, values (Jones and Wall, 1985) of the mean absorbed doses in some organs in a chest examination are given, normalized to the mean absorbed dose in the red bone marrow. The relative absorbed dose values in Fig. 18 are not very sensitive to variations in beam quality. In the figure, measured values from Bengtsson *et al.* (1978) are also indicated and show quite good agreement. The data of Bengtsson *et al.* are mean values from a large number of measurements on patients at 13 hospitals in Sweden in examinations of the lungs and ribs. The technical parameters and projections used in the examinations included by Bengtsson *et al.* are not described and may vary among hospitals.

Gibbs *et al.* (1988) used Monte Carlo calculations to derive organ mean absorbed doses in dental radiography. The organs and their tissue compositions were defined from CT images of a female cadaver. These calculations for a full-mouth intraoral examination compare surprisingly well with corresponding mean absorbed doses measured (Stenström *et al.*, 1986b) using thermoluminescent LiF dosimeters and a head phantom for comparable radiation quality (65 and 70 kVp, respectively), beam geometry (rectangular collimation), and film sensitivity. The largest discrepancy, a factor of 5, occurs for the mean absorbed dose in the thyroid. Since the thyroid is outside the primary beam, this value is very sensitive to the position of the fields. For organs represented within the primary beam (red bone marrow, bone surfaces, lymphoid tissues, brain, and

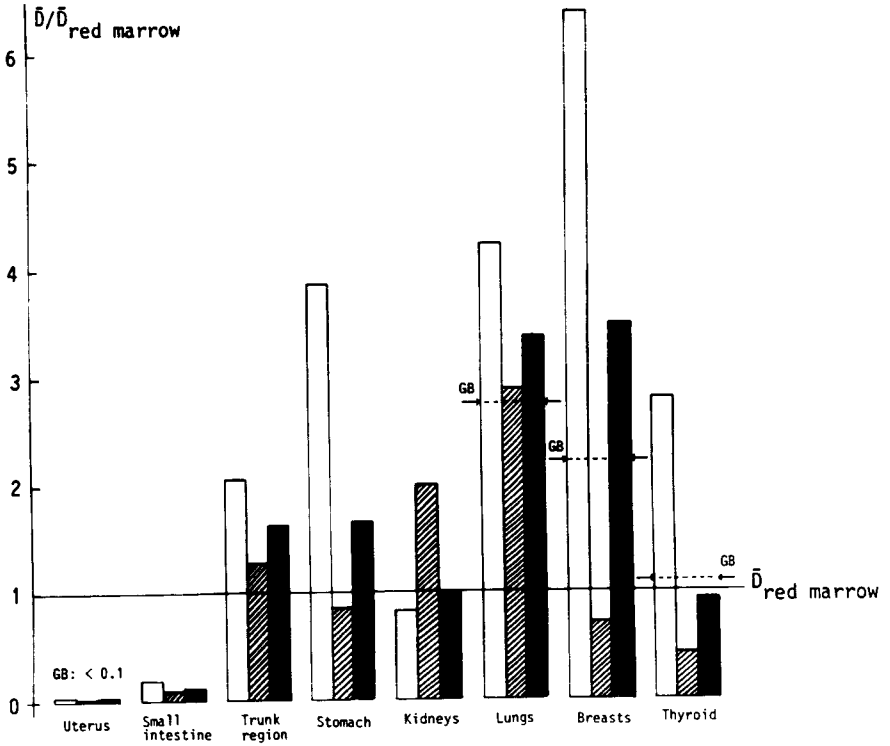

Fig. 18. Mean absorbed doses in various organs, normalized to that in the red bone marrow, in a chest examination; 140 kV, 4-mm Al total filtration (Jones and Wall, 1985). The values, measured by Bengtsson *et al.* (1978) and indicated with GB, are averages over the projections of a complete examination. Open, shaded, and filled bars stand for AP, PA, and LAT projections, respectively.

sinus epithelium), the measured values are within 70% of the calculated ones. Regarding salivary tissues, Stenström *et al.* consider both the parotid gland (outside the primary beam) and "remaining salivary glands" (inside the primary beam). Gibbs *et al.* do not specify their "salivary gland," making comparison inconclusive.

Monte Carlo calculated values of absorbed doses do not include contributions from leakage radiation from the x-ray tube assembly and radiation scattered outside the patient. For organs within the primary beam, this is of minor importance. For organs situated several centimeters from the primary beam, Rosenstein (1976) concludes that, in neglecting the stray radiation, absorbed doses may be underestimated by 25–50%.

C. Mammography Dosimetry

Due to the low photon energies used in mammography, the tissue composition strongly influences the mean absorbed dose in (or energy imparted to) the breast in an examination (Hammerstein *et al.*, 1979; Stanton *et al.*, 1984; Kulkarni and Supe, 1984; Rosenstein *et al.*, 1985). Adipose and glandular tissues are the main components. The fraction of adipose tissue generally increases with increasing age. The preferred quantity for assessing radiation risk from x-ray mammography is the mean absorbed dose in glandular tissue, excluding the skin layer (ICRP, 1987b).

Nielsen and Fagerberg (1986) determined the spread in tube charge (amperesecondes) used in examining 80 women during 1 day of mammography screening, using roentgen radiation generated with 25-kV constant acceleration voltage and a Mo target. For the same film optical density, the values ranged from 25 to 190 mAs, demonstrating the large variation in breast tissue compositions and thicknesses.

The accuracy in determining either the energy imparted to the breast or the mean absorbed dose in the breast for individual patients is thus severely limited. The conversion factors needed to derive the energy imparted to the breast (Doi and Chan, 1980; Dance, 1980) from knowledge of $\int_A K_{c,air}\, dA$ (Section V,B,3) depend on tissue composition, which cannot be known for the individual patient. Determination of the mean absorbed dose in the breast or in its glandular tissues is still more complicated, because it also requires knowledge of the mass of the patient's breast ($\bar{D} = \varepsilon/M$).

As a consequence, when comparing mammographic techniques for screening procedures, standardized breast phantoms must be used. The most commonly used reference composition for an "average" breast of women above 40 years of age is a 50 : 50 mixture by weight of adipose and glandular tissues, closely approximated by a 50 : 50 mixture by weight of fat and water (Boag *et al.*, 1976; Hammerstein *et al.*, 1979; Doi and Chan, 1980; Dance, 1980; Stanton *et al.*, 1984; Jones and Wall, 1985; Rosenstein *et al.*, 1985). This is also the reference composition recommended by the ICRP (1987b). Materials equivalent to the "average" breast tissue have been described (White, 1977b; White *et al.*, 1977).

Mean absorbed doses in an average breast or its sensitive (glandular) tissue have been derived either from measurements of depth–ionization curves or from calculations of ε. Usually, the values are normalized to the incident exposure, free in air at the entrance field.

Stanton *et al.* (1984) measured the exposure from primary and forward-scattered photons transmitted through various thicknesses of a semicircu-

lar, average breast phantom (BR 12). Appropriate exposure backscatter factors (Stanton *et al.*, 1982) were applied to derive the total exposure at a depth within the phantom. Full backscatter was included at all depths, yielding a universal depth–exposure curve, used for all breast thicknesses. A depth-independent conversion factor from exposure to absorbed dose (f factor) was applied to derive absorbed doses at depth.

Hammerstein *et al.* (1979) determined depth–exposure curves in an average breast (BR 12) phantom, using calibrated thermoluminescent LiF dosimeters ($3.2 \times 3.2 \times 0.9$ mm^3). Due to the finite thickness of the dosimeters and the change in the energy distribution of the primary photons with depth, the TL-to-exposure conversion factor varies (by up to 15%) with depth and was corrected for with the softer beams. At all depths, backscatter from a 1-cm-thick layer of the phantom was also included by Hammerstein *et al.*

Stanton *et al.* (1981) compared depth–exposure curves in an average breast phantom, as measured by an ionization chamber and the same LiF–TL dosimeters as used by Hammerstein *et al.* (1979). The TL-to-exposure calibration factors (given as a function of HVT) of Hammerstein *et al.* (1979) were used in combination with HVT measurements of the primary photons as a function of depth. The depth–exposure curves, obtained with the TL dosimeters, show a tendency to be less steep than those obtained with the ion chamber. The TL-to-exposure calibration factors given by Hammerstein *et al.* are determined for the incident primary photons and fail to account for the effects of scattered photons when the dosimeters are irradiated within a phantom. The thick TL dosimeters tend to underestimate the fluence of backscattered photons compared to that of the perpendicularly incident primary photons (Alm Carlsson and Carlsson, 1982), resulting in an underestimate of the backscatter factor. The magnitude of this underestimate has been investigated in Monte Carlo calculations by Chan and Doi (1981). A systematic error in the ionization chamber measurements may arise from using backscatter factors for perpendicularly incident photons to derive the total exposure at a depth (cf. Stanton *et al.*, 1984). The forward-scattered photons have an angular distribution which further enhances backscatter (Persliden and Alm Carlsson, 1984).

The mean absorbed dose in the breast has also been derived from Monte Carlo calculations (Doi and Chan, 1980; Dance, 1980; Kulkarni and Supe, 1984; Rosenstein *et al.*, 1985) and by measurements (Shrivastava, 1981) of ε ($\bar{D} = \varepsilon/M$).

Doi and Chan (1980) used a laterally infinite phantom and perpendicularly incident photons. Dance (1980) used more realistic modeling of the compressed breast, simulating varying thicknesses, various finite lateral extensions, and a finite focus-to-skin distance (FSD) of 75 cm. In the model, a 3-mm-thick compression plate of Perspex above the breast is included as well as the detector (selenium plate) and its Perspex support behind the breast. Results, normalized to unit entrance exposure free in air behind the compression plate, are shown in Fig. 19. In the figure, corresponding values for a 5-cm-thick breast according to Doi and Chan (1980) are included. At low photon energies the agreement is good, but at 28.5 keV the value of Doi and Chan is 30% above that of Dance. The lateral escape of radiant energy, caused by the finite slab and divergent beam used by Dance, increases with increasing photon energy and is the main reason for the discrepancy (D. R. Dance, personal communication, 1988).

Mean absorbed doses from Dance (1980) are in close agreement with those of Hammerstein *et al.* (1979) determined from the measured depth–exposure curves cited above (FSD = 45–49 cm). This is true for the mean absorbed dose in the entire breast as well as in its glandular tissues.

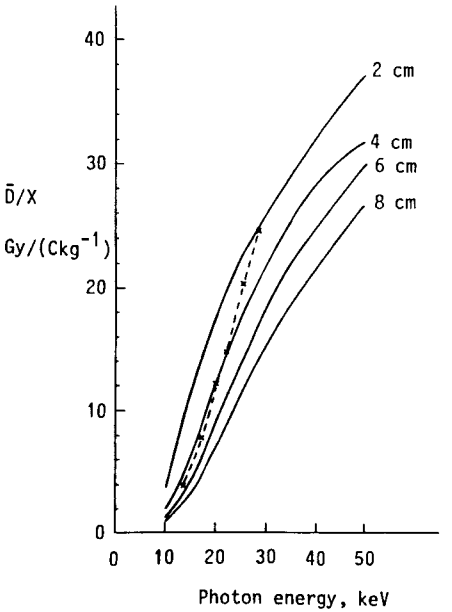

Fig. 19. Mean absorbed dose in the entire breast, $\bar{D}$, per unit entrance exposure, X, free in air, for 2-, 4-, 6-, and 8-cm-thick compressed breasts of medium area, 0.93×10^{-2} m^2 (Dance, 1980) as a function of photon energy (focus–skin distance 75 cm). (Dashed line) Values for a 5-cm-thick breast assuming laterally infinite extension (Doi and Chan, 1980) and perpendicular photon incidence. Breast composition: 50:50 mixture by weight of fat and water.

To avoid uncertainties in calculating the f factor for the breast, to be used in converting depth–exposure curves to depth–dose curves, Shrivastava (1981) suggested determination of ε from measurements of entrance and exit exposures. Although depth–exposure curves measured by Shrivastava in a BR 12 phantom are very close to those of Hammerstein *et al.* (1979), his values of the mean absorbed dose in the breast are considerably higher and largely agree with those of Doi and Chan (1980) (Fig. 20A).

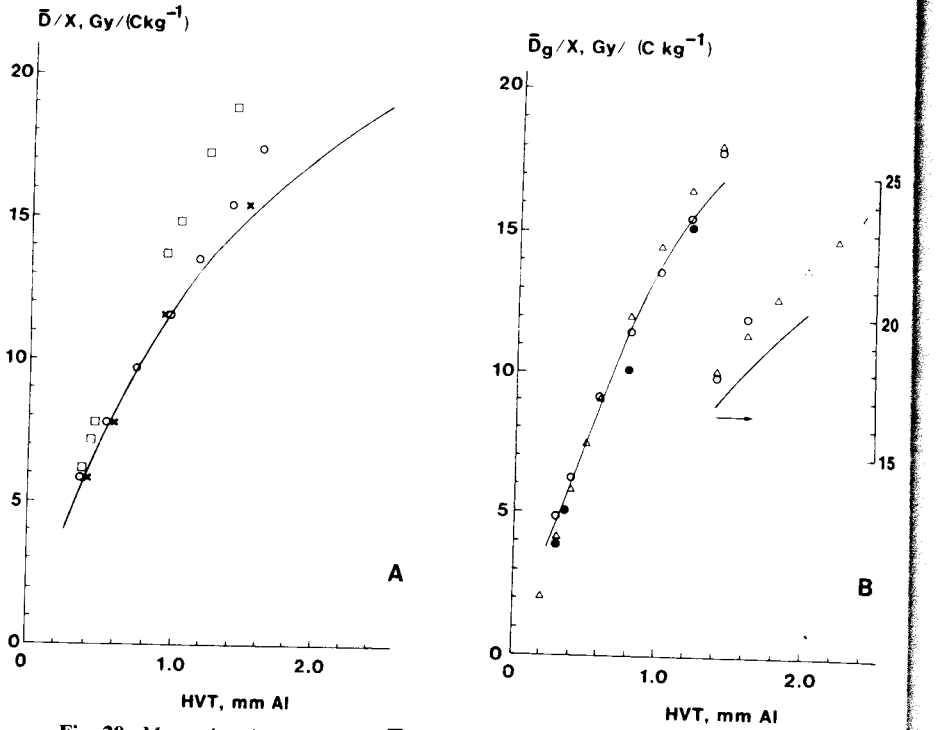

Fig. 20. Mean absorbed doses (A) $\bar{D}$ (whole breast) and (B) $\bar{D}_g$ (glandular tissue) in a 6-cm-thick firmly compressed breast (50:50 fractions by weight of glandular and adipose tissues) as a function of HVT, normalized to unit entrance exposure, X, free in air. (A) Dance (1980): (———) FSD = 75 cm; Stanton *et al.* (1984): (○) depth exposure measurements, FSD = 55–72 cm, and (×) energy fluence method using imparted fractions from Dance (1980); Doi and Chan (1980): (□) laterally infinite slab geometry, FSD = ∞. (B) D. R. Dance (personal communication, 1988): (———) (5-mm adipose shield, FFD = 60 cm; Stanton *et al.* (1984): (○) 5-mm adipose shield, FSD = 55–72 cm, depth exposure measurements; Rosenstein *et al.* (1985): (△) 4-mm glandular tissue shield, FFD = 76.2 cm; Hammerstein *et al.* (1979): (●) 5-mm shield, homogeneous phantom, FSD = 45–49 cm, depth exposure measurements. Abbreviations: FSD, focus–skin distance; FFD, focus–film distance.

The consistency of the Monte Carlo calculations by Doi and Chan (1980) and Dance (1980) (Fig. 19) and the results of Hammerstein *et al.* and Dance (Fig. 20) for similar beam and phantom geometries suggests that this agreement is probably fortuitous. In using central-axis exposure values, Shrivastava (like Chan and Doi) underestimates the lateral escape of radiant energy from the finite-sized breast, but this also applies to the results of Hammerstein *et al.* The basic equations used by Shrivastava to derive ε assume a parallel, perpendicularly incident beam and a lateral balance of in- and outscattering of radiant energy for the volume considered (a circular column at the center of the phantom). With a divergent beam, the relevant volume for the determination of energy imparted changes from a circular column to a cut cone with a comparatively larger volume. Another difficulty concerns the conversion of values of exposure X to values of the plane energy fluence Ψ_{pl} (see Section IX), which presupposes detailed knowledge of the angular and energy distributions of both incident and escaping photons (Alm Carlsson, 1985). With the low-energy photons in mammography, weighted averags of $(\mu_{en}/\rho)_{air}$ [Eq. (5)] are particularly sensitive to the photon energy distribution.

The state of the art of mammography dosimetry is summarized in Fig. 20. Stanton *et al.* (1984) used the f factors 25.6 Gy C^{-1} kg for average breast tissue (Fig. 20A) and 30.6 Gy C^{-1} kg for glandular tissue (Fig. 20B) from Hammerstein *et al.* (1979). In Fig. 20A the values obtained from measured depth doses exceed those from the energy fluence method for HVT > 1.2 mm Al. This may reflect an overestimate caused by using central-axis depth doses for which saturated scatter is approached (see Section V,B,2). The IF values of Dance (used by Stanton *et al.* in the energy fluence method) include the full lateral escape of radiant energy from a finite-sized breast.

In calculating the mean absorbed dose in the glandular tissues (Fig. 20B), these tissues are generally assumed to lie beneath a 4–5-mm shield of nonsensitive tissue (the assumed atomic composition and density of the shield, however, vary). Monte Carlo calculations by Kulkarni and Supe (1984) give values noticeably higher (30–40%) than those in Fig. 20B. Their simulation of a realistic shield composed of pure adipose tissue seems insufficient as an explanation. The results in Fig. 20B give no indication of a large influence of the assumption of the composition of the shield.

In Fig. 20, HVT is used as the only quality-indicating parameter. This seems to be fairly appropriate. However, there is a definite dependence on the exact photon energy distribution. For Mo and Mo/W targets, the mean absorbed doses per unit entrance exposure are systematically ≈5% lower than those for W targets for the same HVT (Stanton *et al.*, 1984).

VII. Absorbed Doses in the Fetus and in Small Children

A. Fetus

Epidemiologists are interested in retrospective studies of the frequency of teratogenic effects, as well as of induced leukemia and cancers, and their relation to diagnostic x-ray examinations. Data on absorbed dose in the fetus are, however, scarce (Hufton, 1979; Ragozzino *et al.*, 1981).

Hammer-Jacobsen (1963) presumed that when pregnant women undergo examinations of regions remote from the gonads, the fetal gonad dose is equal to female gonad dose, which is frequently reported. In the first trimester the fetus can, in such cases, be regarded as homogeneously irradiated, and reported absorbed doses in female gonads may be used for epidemiological studies. Wall *et al.* (1988) conclude that the mean absorbed dose in the fetus during the first trimester can be approximated by the mean or midpoint absorbed dose in the uterus. Ragozzino *et al.* (1986) measured the depth from the anterior maternal surface to the midline of the fetal skull and abdomen in 97 pregnant women. Their data enable a reasonable estimate of absorbed doses in fetal brain, abdomen, and whole body for mothers of different shape, size, and gestational age.

B. Children

There is no fundamental difference between the method used to determine mean organ absorbed doses in children and that used in adults. For all indirect measurements there is, however, a need for appropriate phantoms and knowledge of the distribution of active bone marrow. Kereiakes and Rosenstein (1980) used physical and mathematical phantoms for measurements with TL and Monte Carlo calculations, respectively. Cristy (1981a) designed a series of mathematical phantoms for estimates of organ mean absorbed doses from internal radiation sources. These phantoms can equally well be used for Monte Carlo calculations of mean absorbed doses in organs from external x rays. The same author (Cristy, 1981b) gives the fractional volume of different body regions as a function of age and also the content of active marrow in a given bone, expressed as a percentage of the total active marrow in the body and as a function of age. François *et al.* (1988) developed a model based on the metric science of growth (auxology) for determining the location of a large number of organs in children. The relevant input parameters are the child's sex and height. Their numerical data refer to the present French population.

VIII. Dosimetry in Computerized Tomography

There are some reasons for a separate section treating patient dosimetry in computerized tomography. Ordinary central-projection radiography and CT differ in a number of aspects, discussed below.

A. Primary Spectra

With the exception of lung examinations, CT as a rule uses higher photon energies than ordinary radiography. The reason for this is that in the projection ray or line integral p [Eq. (31)], the linear attenuation coefficient μ of a volume element should have the same value for all projection rays through this volume element. This linearity condition is strictly valid only for monoenergetic photons.

$$p = \int_L \mu(h\nu)\, dL \tag{31}$$

The linear attenuation coefficient μ depends on photon energy $h\nu$, density, and atomic composition. L is the thickness of the object in the direction of the ray. The nonlinearity of Eq. (31) with an energy spectrum is most pronounced when photoelectric absorption dominates the attenuation. By increasing the primary filtration and the acceleration voltage, incoherent (Compton) scattering, which depends less on energy and atomic number, will dominate μ. This results in greater linearity of the projection and fewer spectral-hardening artifacts, at the expense of decreased contrast and increased radiation risk, H_E (see Section X).

B. Attenuation-Equalizing Filters

Compensating filters used in radiography for increasing image quality and reducing absorbed doses in the patient, as illustrated in Fig. 21 (Edholm and Jacobson, 1971a,b), also reduce the spectral-hardening artifacts in CT. In CT machines, however, the compensating filters are often placed on both sides of the patient. From a dose-minimization viewpoint, all filters used for spectral shaping or attenuation equalizing should be placed on the tube side of the patient.

C. Scattered Radiation

The scanning-ray or fan-beam geometries used in CT are most favorable for maximizing the information-to-risk ratio because most of the scattered radiation behind the patient does not hit the detectors. This reduces the absorbed doses required to obtain a given amount of information.